ANL-09/31

Argonne NATIONAL LABORATORY

U-Mo Fuels Handbook

Version 1.0

Nuclear Engineering Division

ANL-09/31

U-Mo Fuels Handbook

Version 1.0

prepared by
J. Rest, Y. S. Kim, G. L. Holmes
RERTR Program
Nuclear Engineering Division, Argonne National Laboratory

and

M. K. Meyer, S. L. Hayes
Idaho National Laboratory

June 2006

U-Mo Fuels Handbook
Version 1.0

Compiled by

J. Rest, Y. S. Kim, G. L. Hofman
Argonne National Laboratory

and

M. K. Meyer and S. L. Hayes
Idaho National Laboratory

RERTR Program
Argonne National Laboratory

June 2006

Argonne National Laboratory, Argonne, Illinois, 60439

This work was supported by the U.S. Department of Energy, Office of Global Threat Reduction (NA-21), National Nuclear Security Administration, under Contract No. DE-AC-02-06CH11357 between UChicago Argonne, LLC and the Department of Energy.

Intentionally Blank Page

Table of Contents

PREFACE

Conversion of high-performance research reactors in the U.S. and abroad to the use of LEU (low-enriched uranium) fuel requires large increases in uranium densities in the fuel meat of their various fuel plates. In addition, conversion of some lower-power research reactors to the use of LEU fuels requires uranium densities substantially higher than those possible with U_3Si_2 dispersion fuel. Because the high-uranium-content compounds (e.g., U_3Si and U_6Fe) previously have been shown to be unstable under irradiation in fuel plates, the emphasis for US-RERTR advanced fuel development has been placed on metallic uranium of low alloy content for both monolithic and dispersion fuel designs.

Since 1997, several irradiation tests of U-Mo dispersion fuels have been conducted by the Canadian, French, Korean, and U.S. research reactor fuel development programs. These tests have shown that in terms of irradiation behavior, U-Mo alloys are the best candidates for the dispersed fuel phase.

U-Mo alloys were extensively studied in the 1960's as fast reactor fuels and for use in fast burst reactors. Since fast reactor fuel irradiation experiments were conducted at high temperature, the irradiation performance database generated as a result of this work is only marginally applicable to the current issue of research reactor fuel development. In addition to irradiation testing, however, a large amount of work was completed on determination of phase equilibrium, transformation kinetics, and physical, thermal, and mechanical properties. Since the properties of aluminum alloys are generally well known, the combined databases for Al and U-Mo provide a starting point from which property values for U-Mo dispersions can be estimated by the development and application of appropriate correlations.

Some data cannot easily be estimated, however, which requires that new data be generated. The largest deficiency is in the area of the properties of $(U\text{-}Mo)Al_x$ compounds that form as a result of fuel-matrix interaction (for dispersion fuel) or fuel-cladding interaction (for solid U-Mo, or monolithic, fuel). For example, the thermal conductivity of these compounds has a large bearing on dispersion fuel behavior but has not been measured. The same situation applies in higher aluminide phases, since the nature of the compounds that form as a result of this reaction is not well known. As another example, the mechanical strength of fuel is a strong function of interface properties and processing technique, and requires measurement to establish properties.

Although the use of U-Mo alloys in dispersion fuel enables high-densities to be achieved, a major issue with this fuel is the reaction between U-Mo and matrix Al. It has been shown that under certain irradiation conditions, this reaction product exhibits unstable swelling behavior, resulting in excessive and unpredictable fuel plate swelling. The irradiation behavior of the U-Mo fuel particles themselves, however, has been shown to be stable. Several potential fixes to the fuel performance problems associated with the interaction phase are currently being irradiation tested. The U-Mo monolithic fuel provides the highest possible densities and eliminates the problem of the fuel-matrix reaction; however, a similar problem may arise in the interaction layer formed between the U-Mo and the aluminum alloy cladding.

This handbook provides an overview of property data and fuel performance topics with an emphasis on data available for U-Mo alloys. These data often exist only in report format and have not been widely disseminated in the journal literature. For some topics there is more than one source of data, which are sometimes inconsistent. In this situation, the authors have attempted to select the best dataset to provide a standard for fuel designers and reactor operators. Following the section on unirradiated and irradiated materials properties for the monolithic U-Mo alloy, property data for cladding and matrix aluminum are presented. Property data for cladding aluminum are more widely available, and are not presented in great depth. Finally, some properties of (U-Mo)/Al dispersions are also included in this document. Where no data are available, best estimate correlations are provided. Best fits to the data are presented in order to facilitate use by fuel designers and reactor operators.

In some cases (especially for irradiated materials properties), model correlations must be used to estimate the properties where no data are available and compared to data where they exist. As further properties data become available, correlations will be improved and used to better model U-Mo fuel performance. This document will be revised periodically to include new and improved data and correlations.

SECTION 1 GENERAL

1.1 Unit Conversion

Throughout this report SI (i.e., metric) system units are preferentially used. Where more consistent, cgs units are also used. Where data are presented as culled from the literature, the following unit conversions are used or can be applied.

Mass

1 lb = 0.45359 kg

Length

1 cm = 0.01 m
1 in. = 0.0254 m
1 ft = 0.3048 m

Temperature

The basic unit for temperature is the absolute temperature in Kelvin (K), which is related to the Celsius scale by

T (K) = T (^{o}C) +273.15

Temperatures in degrees Fahrenheit (^{o}F) are converted to the Kelvin scale as follows:

$$T(K) = \frac{5}{9}\left[T(^{o}F) - 32\right] + 273.15$$

Pressure

1 atm = 101,325 Pa
1 atm = 760 torr
1 bar = 100,000 Pa
1 torr (mm Hg) = 133.322 Pa
1 psi = 6,895 Pa

Energy,

1 cal = 4.184 J
1 Btu = 1055 J
1 MeV = 1.602×10^{-13} J

Thermal Conductivity

1 Btu/hr-ft-^{o}F = 1.731 W·m^{-1}K^{-1}
1 cal/sec-cm-^{o}C = 418.7 W·m^{-1}K^{-1}

Fission Density, Burnup

A useful, approximate relationship between burnup B, defined as U-235 depletion, and fission density FD is obtained by Snelgorve [1]:

$$FD = (2.15 \times 10^{21})\ \rho_U\ e\ B/FF \quad \text{fissions/cm}^3,$$

where ρ_U is the uranium density in the fuel particle or fuel meat, depending on which fission density is being calculated, e is the uranium enrichment, and FF is the fraction of fissions occurring in U-235. Values of FF appropriate for typical MTR-type reactors are listed in Table 1.1 as a function of burnup for three enrichments. The values of FF for other burnups and enrichments can be estimated by interpolation.

Table 1.1 FF as a function of burnup and enrichment.

	Enrichment				Enrichment		
Burnup	0.1975	0.45	0.93	Burnup	0.1975	0.45	0.93
0.000	0.9958	0.9978	0.9997	0.525	0.9443	0.9670	0.9958
0.025	0.9933	0.9961	0.9995	0.550	0.9414	0.9652	0.9956
0.050	0.9912	0.9946	0.9993	0.575	0.9385	0.9633	0.9953
0.075	0.9889	0.9931	0.9991	0.600	0.9353	0.9617	0.9951
0.100	0.9866	0.9918	0.9990	0.625	0.9322	0.9597	0.9949
0.125	0.9841	0.9902	0.9988	0.650	0.9288	0.9578	0.9946
0.150	0.9819	0.9888	0.9986	0.675	0.9251	0.9559	0.9944
0.175	0.9795	0.9874	0.9984	0.700	0.9214	0.9539	0.9941
0.200	0.9771	0.9860	0.9982	0.725	0.9176	0.9518	0.9939
0.225	0.9748	0.9847	0.9981	0.750	0.9134	0.9495	0.9936
0.250	0.9722	0.9832	0.9979	0.775	0.9090	0.9470	0.9933
0.275	0.9700	0.9819	0.9977	0.800	0.9043	0.9444	0.9929
0.300	0.9678	0.9806	0.9975	0.825	0.8992	0.9416	0.9926
0.325	0.9654	0.9791	0.9973	0.850	0.8935	0.9383	0.9921
0.350	0.9630	0.9778	0.9972	0.875	0.8869	0.9349	0.9917
0.375	0.9606	0.9763	0.9970	0.900	0.8792	0.9311	0.9912
0.400	0.9579	0.9748	0.9968	0.925	0.8709	0.9266	0.9907
0.425	0.9553	0.9732	0.9966	0.950	0.8617	0.9210	0.9899
0.450	0.9538	0.9718	0.9964	0.975	0.8500	0.9141	0.9891
0.475	0.9500	0.9701	0.9962	1.000	0.8310	0.9015	0.9875
0.500	0.9472	0.9685	0.9960				

1.2 Fundamental Constants

Table 1.1. Fundamental Constants.

Symbol	Quantity	Value
R	Gas constant	8.314 J/mole-K
N_A	Avogadro's Number	6.02217×10^{23} mole^{-1}

1.3 Elemental Data

Table 1.2. Elemental Data [2].

Element	Atomic Number	Atomic mass [a]	Nominal density [b] (g/cm^3)
U	92	238.03	19.05
Mo	42	95.94	10.28
Al	13	26.982	2.70

a : based on ^{12}C=12.0000
b: at 293 K

1.4 References for Section 1

1. J.L. Snelgrove, Private communication, 2006.
2. N.N. Greenwood and A. Earnshaw, Chemistry of the Elements, 2nd edition, Butterworth, UK (1997).

Intentionally Blank Page

SECTION 2 PHYSICAL AND THERMAL PROPERTIES OF U-Mo ALLOY

2.1 Heat Capacity

Values for the heat capacity of U-10Mo alloy have been reported by Farkas [1] and are listed in Table 2.1. The data are plotted in Fig. 2.1, along with values for aluminum. Regression analysis of the data in Table 2.1 in the range of 273-773K yields Eq. (2.1) also plotted in Fig. 2.1. Heat capacity is given in units of J/mol-K.

$$C_P^{UMo} = 29.84 - 8.90\times10^{-3}T + 4.32\times10^{-5}T^2 - 2.06\times10^{-8}T^3 \quad (2.1)$$

Table 2.1. Specific heat capacity of U-10Mo alloy.

Temperature, °C	Heat Capacity, J/mol-K
0	30.1
100	31.7
200	33.3
300	35.0
400	36.7
500	38.3
600	40.0
700	41.7
800	43.2
900	44.9
1000	46.6

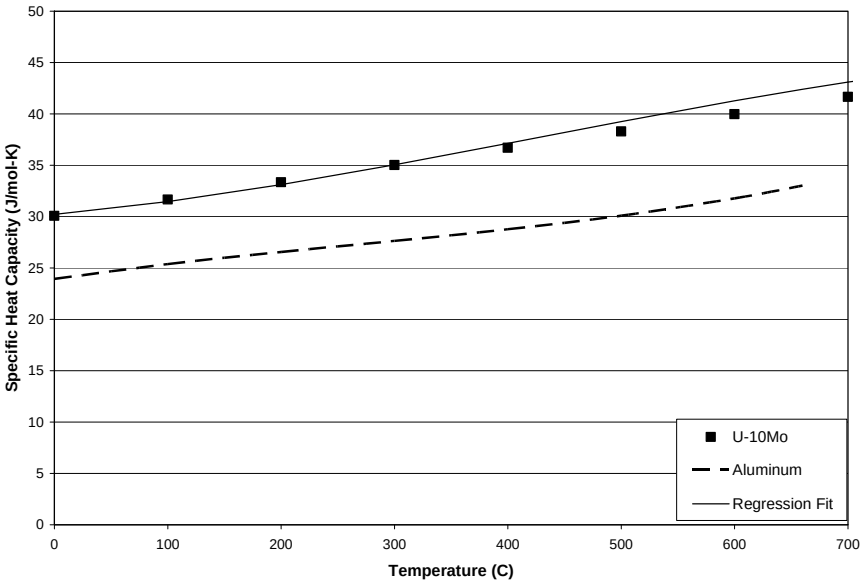

Fig. 2.1. Heat capacity of U-10Mo alloy and aluminum. Upper curve through points represents fit of Eq. (2.1) to U-10Mo data.

2.2 Thermal Expansion

Thermal expansion data for γ-phase U-Mo alloys have been reported by several sources [2-6]. These data are plotted in Fig. 2.2. The data are consistent, except for the values from Repas et al. [5], which appear to be high. A linear regression analysis conducted on the remainder of the data in the temperature range of 298-873 K yields Eq. (2.2), which provides the variation in the thermal expansion coefficient with temperature:

$$\alpha_T = 7.91 + 1.21 \times 10^{-2} T \tag{2.2}$$

where T is the temperature in K and α_T is in 10^{-6}/K. The thermal expansion coefficient of aluminum, 27.5 10^{-6}/K over the range of 293-773K, is on the order of twice that of U-Mo alloys.

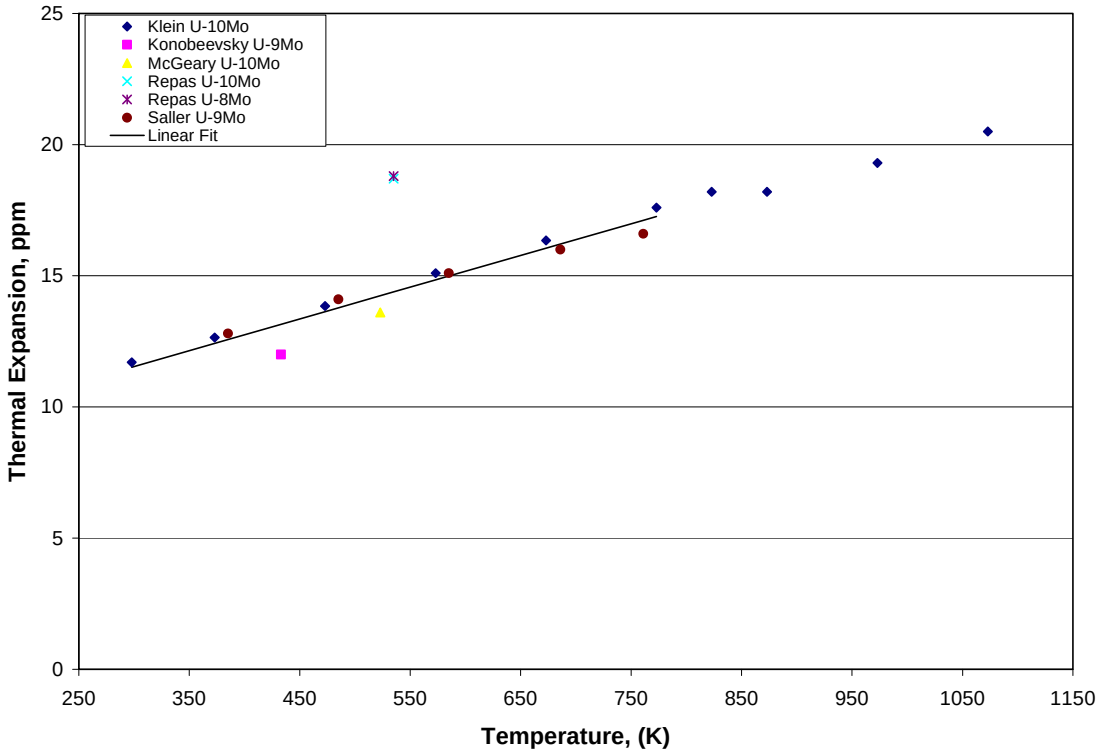

Fig. 2.2. Thermal expansion coefficient of U-Mo alloys. Line represents linear fit to data. Note that all data except that of Klein represent mean values of expansion reported over a temperature range. Data of Klein are 'instantaneous' values.

2.3 Density of U-Mo Alloys

The density of U-Mo alloys has been reported by McGeary [2] as a function of composition for the composition range from 2.5 to 25 wt.% molybdenum. Klein [6] has reported density as a function of temperature for U-10 wt.% molybdenum from 25-550°C. More recently data have been reported by Lee [7] for ingots and Kim [8] for atomized powder. Data for U-Mo alloys from reference [2] are listed in Table 2.2 along with recommended density values for aluminum, uranium, and common fuel compound phases. The uranium density of the alloys falls rapidly with increasing molybdenum content.

The density of γ-phase U-Mo alloys is well represented by a molar rule of mixtures given by Eq. (2.3).

$$\rho_{U-Mo} = X_{Mo}\rho_{Mo} + (1 - X_{Mo})\rho_{U} \tag{2.3}$$

Here X_{Mo} is the molar fraction of Mo in U-Mo alloy and ρ is the density. On the basis of molar fraction, density values calculated using Eq. (2.3) are plotted with the density data from Table 2.2 in Fig. 2.3. It can be seen from Fig. 2.3 that the data of McGeary and Klein are well represented by the rule of mixtures formulation in the range of molybdenum contents from 11.5 at.% (5 wt.%) to at least 21.6 at.% (10 wt.%), encompassing nearly the entire range of

γ-phase (meta) stability. The data of Lee and Kim fall below the predicted values. In the case of Kim's data for powder, the lower than expected values are likely due to porosity present as a result of the powder atomization process. No analyzed chemical composition data are given in reference [7], however approximately 3 wt.% of additional molybdenum would have to be present for the data to fall on the calculated curve. Since it is unlikely that this is the case, no explanation for this discrepancy is available.

Beyond 30 at.% molybdenum, the single set of measured density values published by [2] is higher than those calculated from Eq. (2.3). In this compositional range, the ordered U_2Mo intermetallic phase forms, and Eq. (2.3) is not valid.

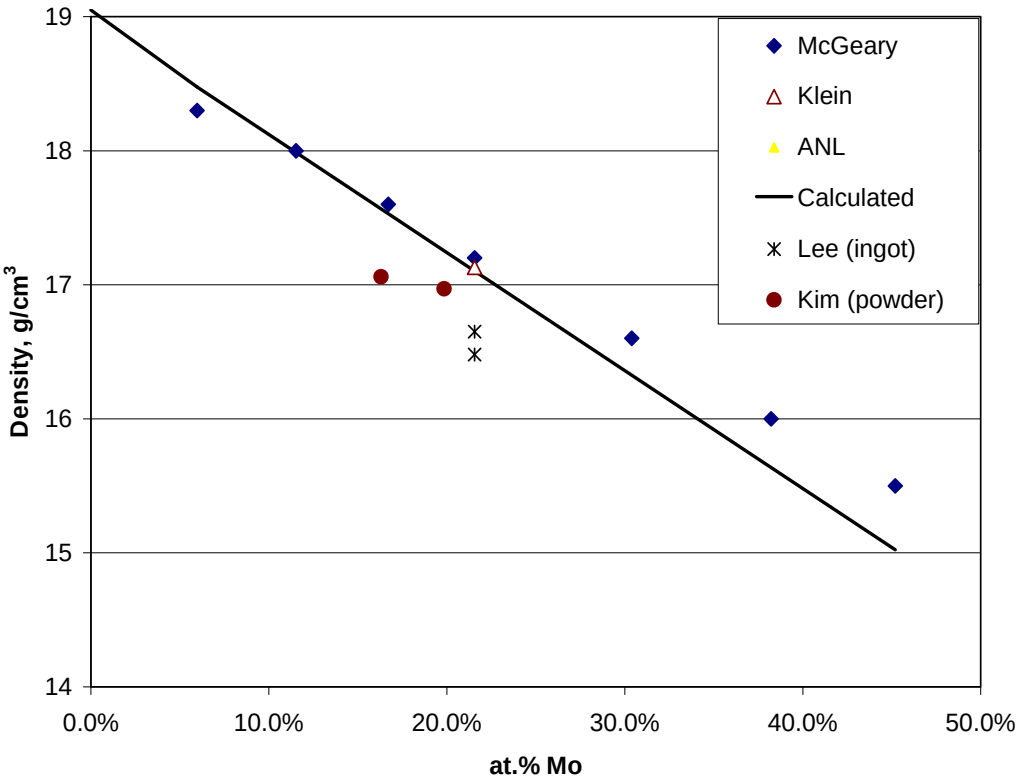

Fig. 2.3. Measured and calculated density data for U-Mo alloys.

Table 2.2. Density data for common fuel compounds, U-Mo alloys, and aluminum.

Material	Density ($g \cdot cm^{-3}$)	Uranium density ($g \cdot cm^{-3}$)
Al	2.70	-
Mo	10.2	-
UAl_4	5.7	3.7
UAl_3	6.8	5.1
UAl_2	8.14	6.63
UAl_x[1]	6.4	4.6
U_3O_8	8.3	7.0
UO_2	10.96	9.67
U_3Si_2	12.2	11.3
U_3Si	15.3	14.7
U_6Fe	17.4	16.7
U-25Mo	15.5	11.6
U-20Mo	16.0	12.8
U-15Mo	16.6	14.1
U-10Mo	17.2	15.5
U-7.5Mo	17.6	16.3
U-5Mo	18.0	17.1
U-2.5 Mo	18.3	17.8
U	19.05	19.05

[1] $10UAl_2+60UAl_3+30UAl_4$

2.4 Lattice Parameter

The variation of the lattice parameter of U-Mo alloys with composition has been provided by Dwight [9] as follows:

$$a_0 = 3.4808 - 0.00314\, x_{Mo} \tag{2.4}$$

where x_{Mo} is the Mo content in U-Mo alloy in atom %.

Figure 2.4 shows the graph of lattice parameter of U-Mo alloys as represented by Eq. (2.4).

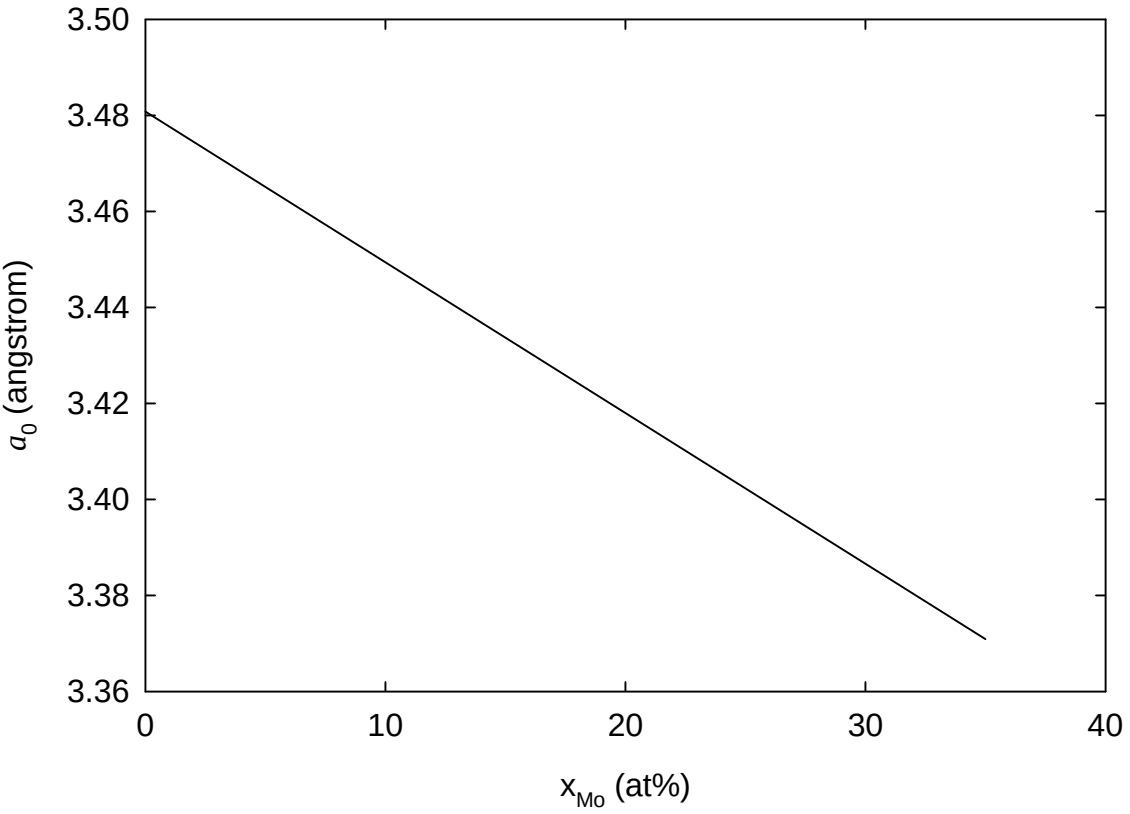

Fig. 2.4. Lattice parameters for U-Mo alloys at room temperature quenched from the γ-phase field as represented by Eq. (2.4) [9].

2.5 Melting Temperature

The solidus line for the U-Mo alloy for the range of the Mo content $0 \le x_{Mo} \le 4\ at\%$ from the U-Mo phase diagram [10] is used to obtain an equation for U-Mo melting temperature as follows:

$$T_m = 1.408 \times 10^3 - 2.912\, x_{Mo} + 0.1606\, x_{Mo}{}^2 \tag{2.5}$$

where x_{Mo} is the Mo content in the U-Mo alloy in atom %, and T_m is in K.

2.6 Thermal Conductivity

Thermal conductivity data as a function of temperature are available from several sources [4, 11-20]. Data are presented in Table 2.3, and plotted in Fig. 2.5. From the plot, it is apparent that the data of Konobeevsky [4] are not in accord with the data from other sources, so these data are not used in developing a correlation for thermal conductivity. The effect of varying alloy content within the range of 6-10 wt.% (likely to be used for U-Mo dispersions) is probably

negligible in comparison to the scatter in the data. The simple linear fit shown by Eq. (2.6) thus provides an approximate representation of the data.

$$K_{U-Mo} \approx 0.032T + 2.2 \qquad 298\ \text{K} < T < 773\ \text{K} \qquad (2.6)$$

Here $K_{U\text{-}Mo}$ is in units of $\text{W}\cdot\text{m}^{-1}\text{K}^{-1}$ and T is absolute temperature.

Table 2.3. Thermal conductivity data for U-Mo alloys.

Comp. (wt.%)	Temp. (°C)	Thermal Conductivity ($\text{W}\cdot\text{m}^{-1}\text{K}^{-1}$)	Reference
U-5Mo	127	22.1	[14,20]
	177	22.8	
	227	23.5	
	277	24.2	
	327	24.9	
	377	25.6	
	427	26.9	
	477	28.2	
	527	29.5	
U-8Mo	10-100	14.2	[13]
U-9Mo	100	16.7	[4]
	200	20.9	
	300	26.8	
	400	32.6	
	500	38.5	
U-9.2Mo	20	14.3	[17]
	100	16.6	
	200	19.4	
	300	22.3	
	400	25.1	
	500	27.9	
	600	31.1	

Table 2.3, continued. Thermal conductivity data for U-Mo alloys.

Comp. (wt.%)	Temp. (°C)	Thermal Conductivity ($W \cdot m^{-1} K^{-1}$)	Reference
U-10Mo	23	12.1	[11]
	100	14.2	
	200	14.2	
	300	17.2	
	400	20.1	
	500	23.0	
	600	26.4	
	700	30.1	
	800	33.9	
	1000	37.7	
U-10Mo	25	9.7	[12]
	100	11.7	
	200	14.0	
	300	17.2	
	400	21.6	
	500	25.7	
U-10Mo	20	12.1	[14]
	100	13.8	
	200	17.3	
	300	20.1	
	400	23.3	
	500	27.2	
	600	30.1	
U-10Mo	50	12.97+1.26	[15]
	212	17.99+2.52	
	308	21.34+2.52	
	404	25.94+4.18	
U-10.7Mo	20	11.9	[18]
	100	14.4	
	200	17.5	
	300	20.6	
	400	23.7	
	500	26.9	
	600	29.9	
U-12Mo	10-100	13.8	[13]

The correlation given in Eq. (2.6) gives a rule-of-thumb estimate for thermal conductivity neglecting the effect of Mo content in the alloy. However, when a more accurate correlation for the effect of the Mo content is needed, the modeling described below is useful.

Touloukian et al. [14] summarized the thermal conductivity data for uranium metal available before 1970. The only data accumulated since then were by Takahashi, et al. [16]. For the temperature range $255 \le T \le 1173\,\mathrm{K}$, the thermal conductivity increased monotonically as temperature increased. A parabolic function of temperature was used to fit the data for U-10Mo. Consequently, the thermal conductivity of uranium metal takes the form

$$k_U(T) = 21.73 + 1.591\times10^{-2}\,\mathrm{T} + 5.907\times10^{-6}\,\mathrm{T}^2 \tag{2.7}$$

where k is the thermal conductivity in $\mathrm{W\cdot m^{-1}K^{-1}}$ and T the temperature in K. The temperature range for Eq. (2.7) was $255 \le T \le 1173\,\mathrm{K}$.

For the thermal conductivity of Mo metal, Touloukian et al. [14] tabulated the recommended values based on assessment of data in the literature. The recommended values showed that the thermal conductivity of Mo decreased linearly as temperature increased for the temperature range of $300 \le T \le 800\,\mathrm{K}$. A linear function of temperature was selected to fit the data. By fitting the data, the thermal conductivity of U-10Mo was obtained as

$$k_{Mo}(T) = 150.0 - 4.0\times10^{-2}\,\mathrm{T} \tag{2.8}$$

where T is in the range of $300 \le T \le 800\,\mathrm{K}$.

Thermal conductivity data of U-Mo alloy are available from Refs. 4, 11 – 20 for the Mo content range of 5 - 12 wt.%. The U-Mo system has the second-phase metallic compound, U_2Mo, at 300 – 800 K, which approximately corresponds to U-17Mo. At this composition, the alloy would have the lowest thermal conductivity. However, because no data were available for the composition and a more conservative approach was deemed necessary, we assumed that the thermal conductivity reached its minimum at 29 wt.% Mo in the alloy. Since no data for U-29Mo were available, U-29Zr data were adopted among U-based alloys with available thermal conductivity [20]. By fitting the data accumulated and prepared above to the following correlation, the thermal conductivity of unirradiated U-Mo fuel was modeled

$$k^0_{U-Mo} = \left(1-\sqrt{1-x_{Mo}}\right)k_{Mo} + \sqrt{1-x_{Mo}}\,\left\{(1-x_{Mo})k_U + x_{Mo}k_{c,Mo}\right\} \tag{2.9}$$

where k^0_{U-Mo} is in $\mathrm{W\cdot m^{-1}K^{-1}}$, x_{Mo} is the Mo content in weight fraction. k_U is given by Eq. (2.7), and k_{Mo} by Eq. (2.8). $k_{c,Mo}$ is a result of the regression analysis of the data to Eq. (2.9) and takes the form

$$\begin{aligned} k_{c,Mo} = {} & -274.4 + 985.2\,x_{Mo} - 1.941\times10^{3}\,x_{Mo}^{\,2} + 3.640\times10^{-2}\,T + \\ & 7.365\times10^{-5}\,T^2 + 5.793\times10^{-2}\,x_{Mo}\,T \end{aligned} \tag{2.10}$$

where T is in K. The valid temperature range is $300 \le T \le 800\,\mathrm{K}$.

No initial porosity was assumed in the unirradiated fuel. Therefore, Eq. (2.9) is not intended to be applicable to a porous U-Mo alloy. Thermal conductivity of U-Mo alloys containing pores is discussed in Section 6.

Fig. 2.5 compares the data used for correlation fitting with the model predictions. The prediction for U-17Mo was also included for comparison. The predictions are generally close to the data.

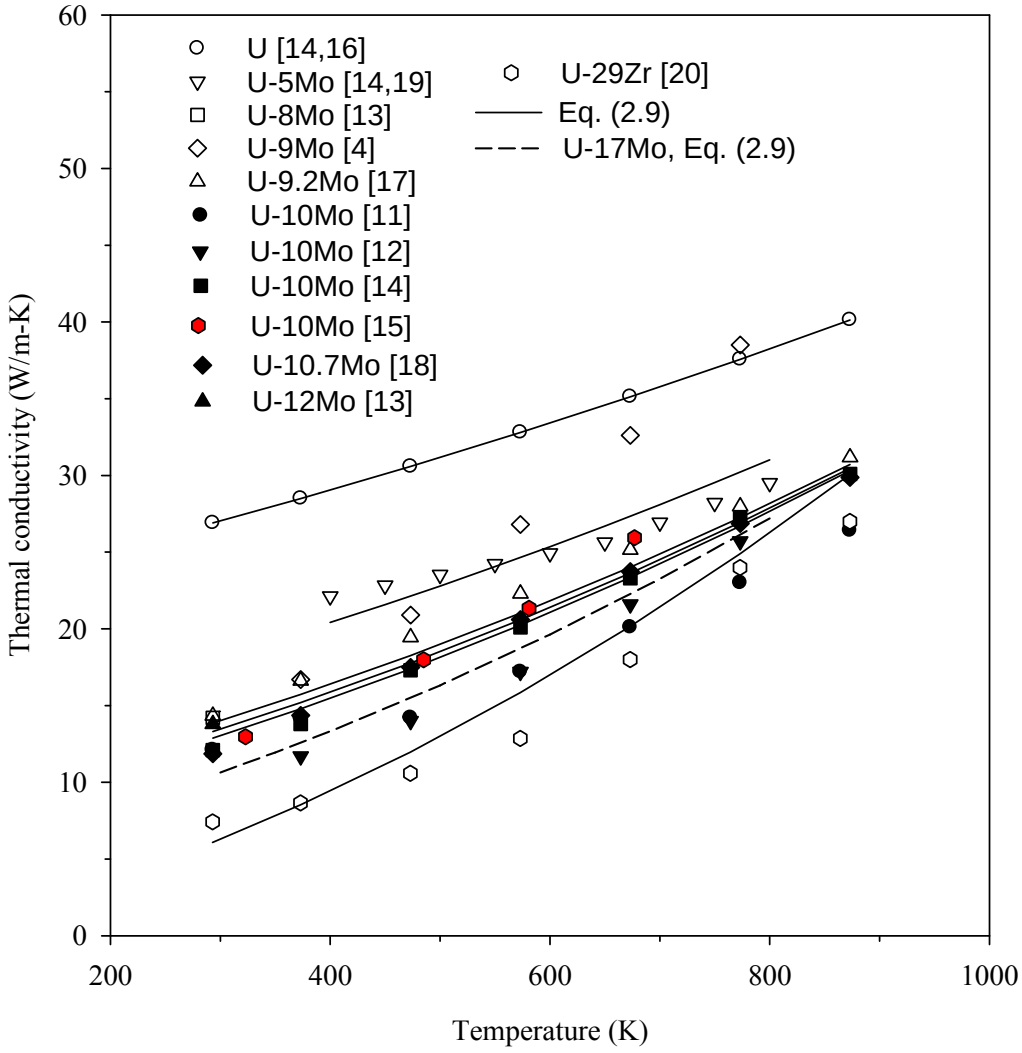

Fig. 2.5 Measured data and model predictions for unirradiated U-Mo alloys. The numbers in front of Mo indicate the Mo content in weight percent.

2.7 References for Section 2

1. Farkas, M.S., "Mechanical and Physical Properties of Fuels and Cladding Materials with Potential for Use in Brookhaven's Pulsed Fast Reactor," Report BMI-X-455 (1967).
2. McGeary, R.K., "Development and Properties of Uranium-base Alloys Resistant to Corrosion in High-Temperature Water," USAEC Report WAPD-127 – Part I (1955).
3. Saller, H.A., Dickerson, R.F., Hurr, W.E., "Uranium Alloys for High-Temperature Application," Report BMI-1098 (1956).
4. Konobeevsky, S.T., "Some Physical Properties of Uranium, Plutonium, and their Alloys," *Proceedings of the Second UN International Conference on the Peaceful Uses of Atomic Energy*, Paper P/2230 (1958).
5. Repas, P.E., Goodenow, R.H., Hehemann, R.F., "Transformation Characteristics of U-Mo and U-Mo-Ti Alloys," Trans. ASM (1964) 150.
6. Klein, J.L., "Uranium and its Alloys," in Nuclear Reactor Fuel Elements, ed. A.R. Kaufmann (1962).
7. Lee, S.-H., Kim, J.-C., Park, J.-M., Ryu, H.-J., Kim, C.-K. , "An Investigation of the Thermophysical Properties of U-Mo Dispersion Fuel Meats," *Proceedings of the 2000 International Meeting on Reduced Enrichment for Research and Test Reactors,* Las Vegas, NV, October 1-6, ANL/TD/TM01-12 (2001).
8. Kim, C.-K., Ryu, H.-J., Park, J.-M., Kim, K.-H., Kim, H.-R., Lee, K.-H., *Proceedings of the 2000 International Meeting on Reduced Enrichment for Research and Test Reactors,* Las Vegas, NV, October 1-6, 2000, ANL/TD/TM01-12 (2001).
9. A.E. Dwight, J. Nucl. Mater., 2(1) (1960) 81.
10. T.B. Massalski, Binary Alloy Phase Diagrams, ASM International, 1990.
11. Klein, J.L., "Uranium and It's Alloys," in Nuclear Reactor Fuel Elements, ed. A.R. Kaufmann (1962).
12. McGeary, R.K., "Development and Properties of Uranium-base Alloys Resistant to Corrosion in High-Temperature Water," USAEC Report WAPD-127 – Part I (1955).
13. Lee, S.-H., Kim, J.-C., Park, J.-M., Ryu, H.-J., Kim, C.-K. , "An Investigation of the Thermophysical Properties of U-Mo Dispersion Fuel Meats," *Proceedings of the 2000 International Meeting on Reduced Enrichment for Research and Test Reactors,* Las Vegas, NV, October 1-6, ANL/TD/TM01-12 (2001).
14. Y. S. Touloukian, R.W. Powell, C.Y. Ho and P.G. Klemens, Thermophysical Properties of Matter, vol. 1, IFI/Plenum, New York (1970).
15. C. Roy, A. Radenac, F. Cado, J. Nucl. Mater., 48 (1973) 369.
16. Y. Takahashi, M. Yamawaki and K. Yamamoto, J. Nucl. Mater., **154**, 141 (1988).
17. T. Matsui, T. Natsume and K. Naito, J. Nucl. Mater., **167**, 152 (1989).
18. .A. Saller, R.F. Dickerson, A.A. Bauer and N.E. Daniel, Properties of a Fissium-Type Alloy, Battelle Memorial Institute, Report BMI-1123 (1956).
19. E.L. Francis, Uranium Data Manual, UKAEA Report IGR-R/R-287 (1958).
20. Yeon Soo Kim and G.L. Hofman, AAA Fuels Handbook, Sect.A-6, Argonne National Laboratory, 2002.

Intentionally Blank Page

SECTION 3 U-Mo PHASES

3.1 U-Mo Phase Diagram

The U-Mo phase equilibrium diagram is shown in Fig. 3.1 [1]. Uranium exhibits only slight solubility of Mo in the α and β phases. The body centered cubic γ phase, however, exhibits a maximum solubility of more than 17 wt.% molybdenum. The γ phase undergoes a eutectoidal decomposition at 565°C, transforming to the orthorhombic α phase and the ordered tetragonal γ′ phase, which has the nominal stoichiometry of U_2Mo. This transformation becomes very sluggish when molybdenum contents are greater than about 6 wt.%, and the alloy can be easily quenched into the γ phase and remain in the γ phase indefinitely at room temperature.

3.2 Metastablility of γ-Uranium Alloys

It is well known that γ-phase uranium alloys exhibit superior irradiation behavior relative to unalloyed uranium. It is also known that, during the elevated temperature fabrication processes used for the manufacture of dispersion fuels, reaction of the fuel with aluminum occurs at a much faster rate for alloys in which α-U is present in the alloy microstructure. These reasons provide the motivation for using a γ-phase uranium alloy as the dispersed fuel phase.

Several transition metals, particularly 4d and 5d elements in Groups IV through VIII, form solid solutions with γ-U, and this cubic phase can be retained in its metastable state upon cooling. The γ stabilizing power of these elements increases with atomic number as d-electrons participate in bonding through hybridization with s and p atomic orbitals. However, their solubility decreases as the size difference with uranium atoms becomes larger, and the increased bond strength promotes intermetallic compound formation. For example, the first two elements in the 4d series, Zr and Nb, form complete solid solutions with γ-U, but U-Zr cannot be retained in the γ phase and U-Nb can be retained in the γ phase only at rather large concentrations. On the other extreme, Pd and Pt have only ~2 at.% solubility and form many very-stable compounds with uranium.

It was recognized early on in the development of fast reactor fuels that molybdenum presents a good compromise between the amount of alloying element needed to stabilize γ-U and acceptable U density so achieved. Some results of these early studies are shown in time-temperature-transformation (T-T-T) diagrams in Fig. 3.2 [2-5]. In these diagrams, the curves represent the time and temperature combinations at which the evidence for the phase transformation is detected. In the case of U-10 wt.% Mo (U-22 at.% Mo) at 500°C, for example, the alloy begins to show signs of transformation after approximately 30 hours. Plotted in Fig. 3.3 is the relationship between γ stability and uranium density for U-Nb, U-Nb-Zr, and U-Mo alloys. Alloys that plot toward the upper right hand corner of the diagram are most desirable, and it is obvious that U-Mo alloys offer the best combination of uranium density in the alloy and γ stabilization. It was further found [5-7] that small amounts of elements to the right of Mo in the periodic table had a powerful stabilizing effect when added to U-Mo alloys.

Data summarizing the effects ternary element additions are shown in Fig. 3.4. Platinum and ruthenium were found to be most effective, and theoretical analysis indicates that osmium

and palladium will act in the same manner. This additional stabilization is gained at no density cost.

3.3 Gamma stability of U-Mo alloy under irradiation

The radiation stability of the U-10 wt.% Mo alloy depends to a considerable extent upon its ability to retain the γ phase during irradiation. When irradiations are conducted at temperatures below ~580°C, this alloy tends to transform to the α and γ′ phases which are thermodynamically stable at these lower temperatures. The effect of fission-induced-displacements and thermal spikes is to oppose this tendency, the spikes tending to disorder the γ′ phase and to produce a homogeneous composition of uranium and molybdenum in the γ phase (see Fig. 3.5). The critical fission rate is that needed to produce the minimum number of displacements and thermal spikes required to maintain the γ phase in opposition to the thermodynamic tendency of the alloy to transform to the α and γ′ phases. This critical fission rate is temperature dependent and decreases with decreasing temperature below the nose of the T-T-T diagram show in Fig. 3.2.

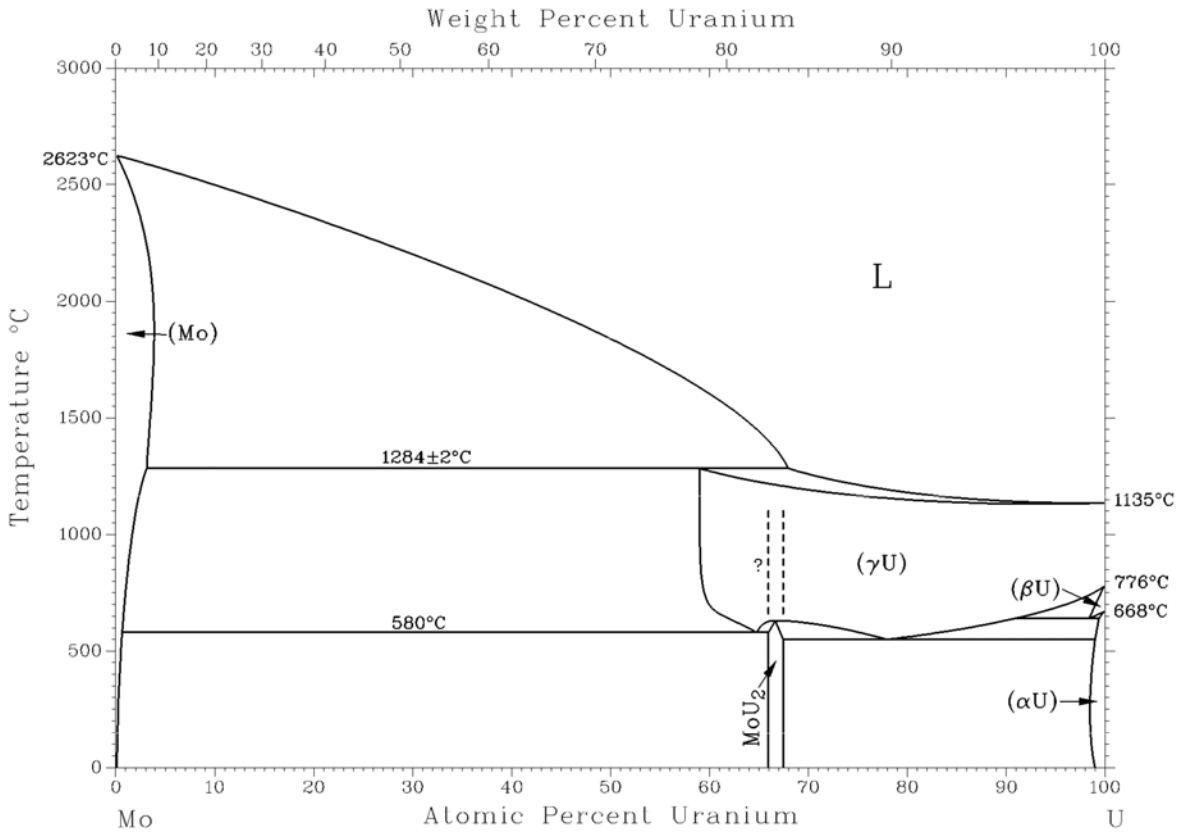

Fig. 3.1. U-Mo phase diagram.

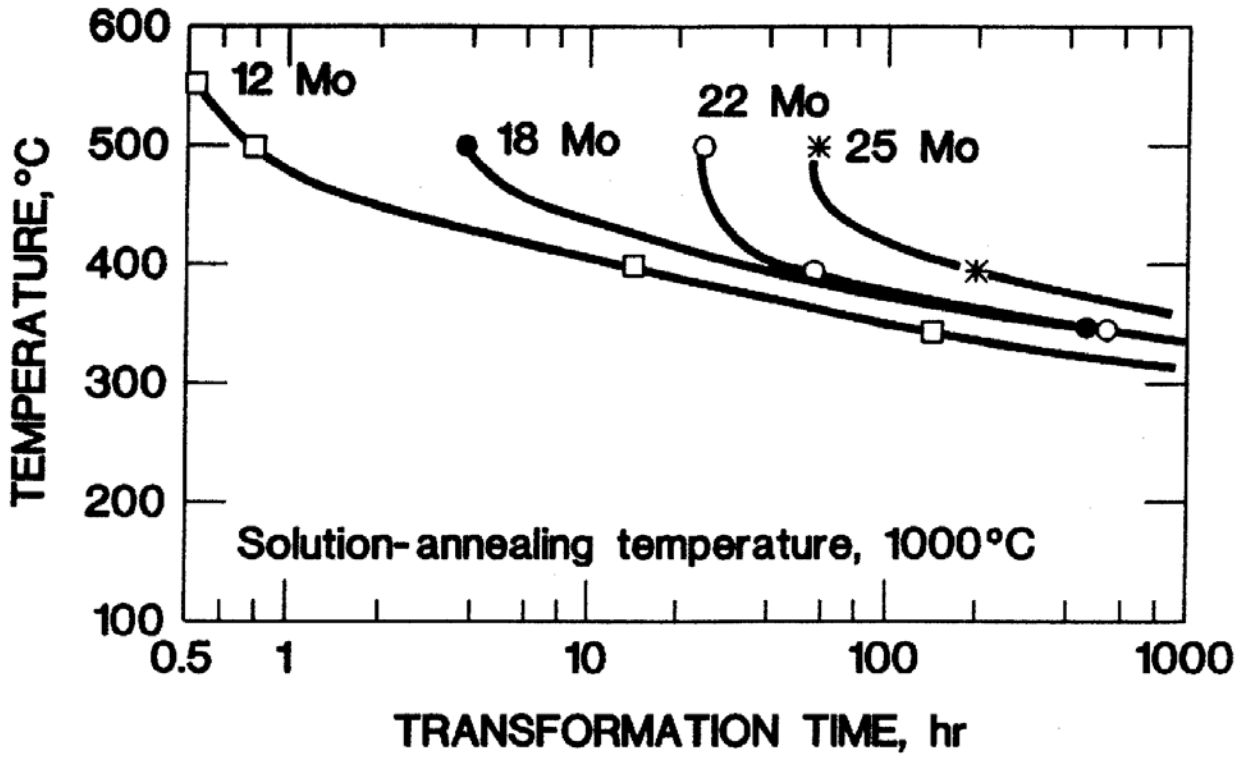

Fig. 3.2. Time temperature transformation curves showing the effect of molybdenum additions on the time to start of eutectoid decomposition of the γ-phase U-Mo alloy after solution annealing at 1000°C.

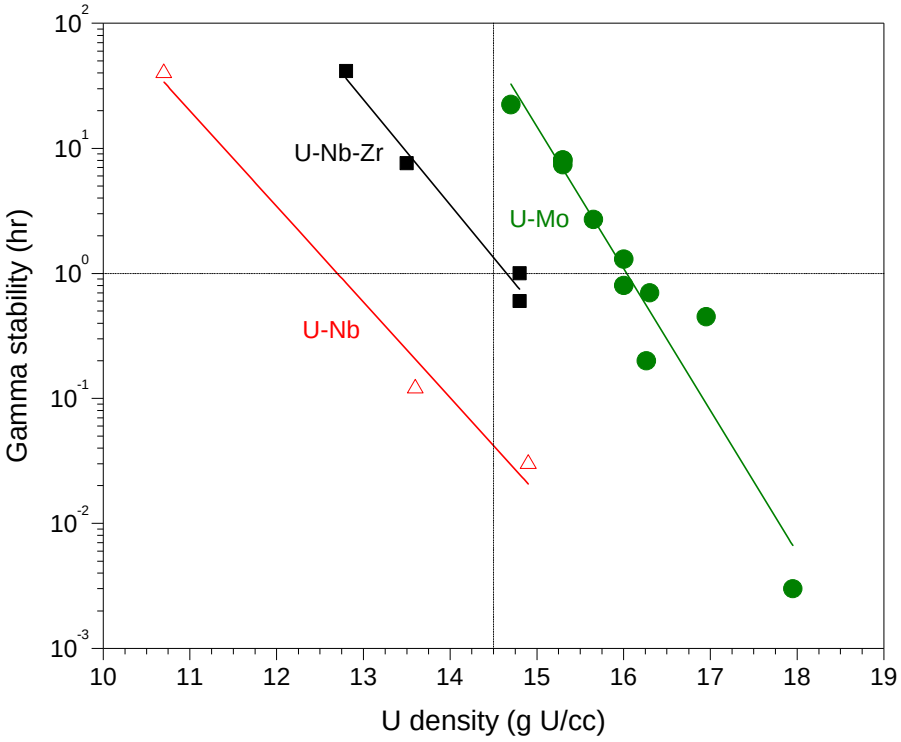

Fig. 3.3. Relationship between γ-phase stability and uranium density for U-Nb, U-Nb-Zr, and U-Mo alloys.

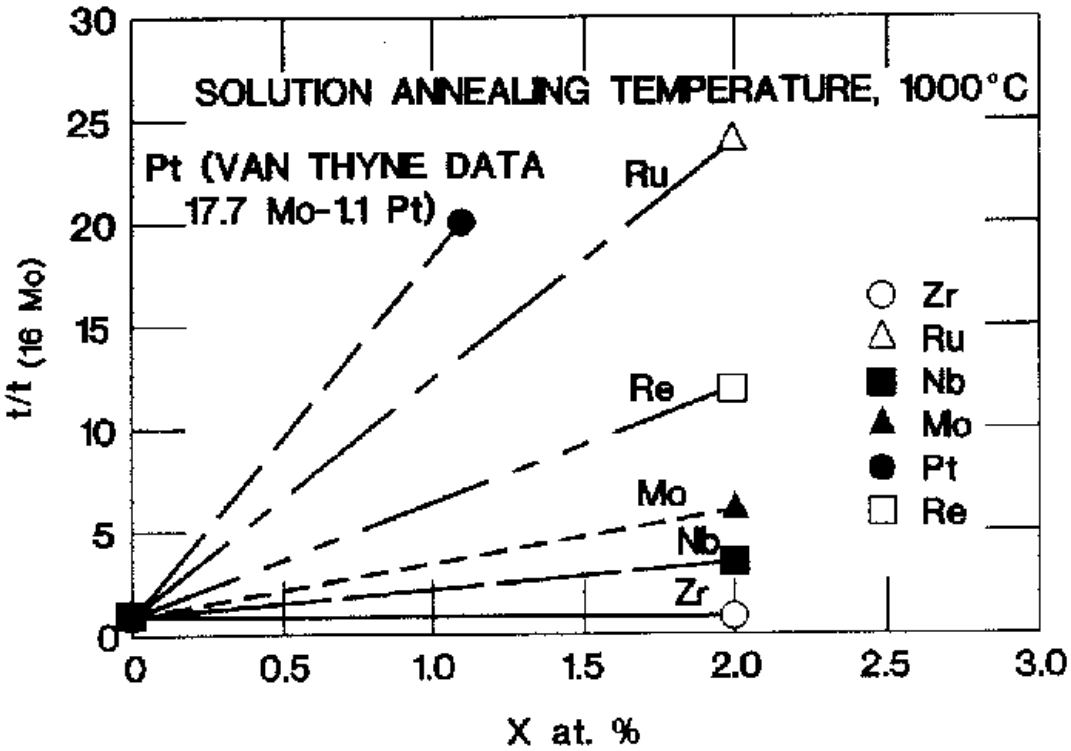

Fig. 3.4. γ-phase stability of U-Mo alloy under irradiation.

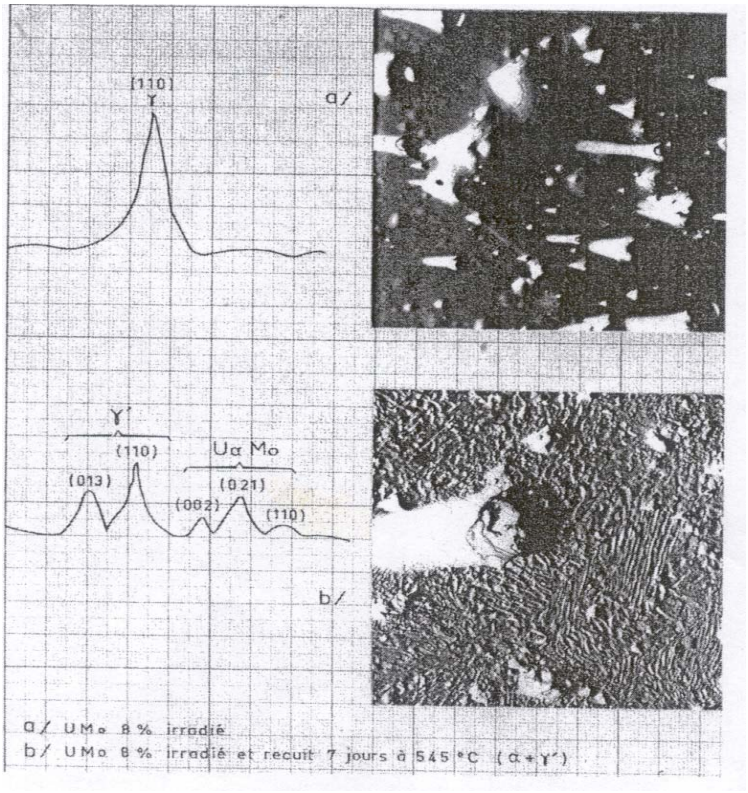

Fig. 3.5 Reversion of $\alpha + \gamma' \rightarrow \gamma$ under irradiation.

The dramatic effect of fission rate on swelling is illustrated in Fig. 3.6, and a clear sample of phase reversal is shown in Feb. 3.7. The fission rates in the RERTR tests are high enough to affect this phase reversal except in the 4% Mo alloy, where the thermodynamic conditions prevail.

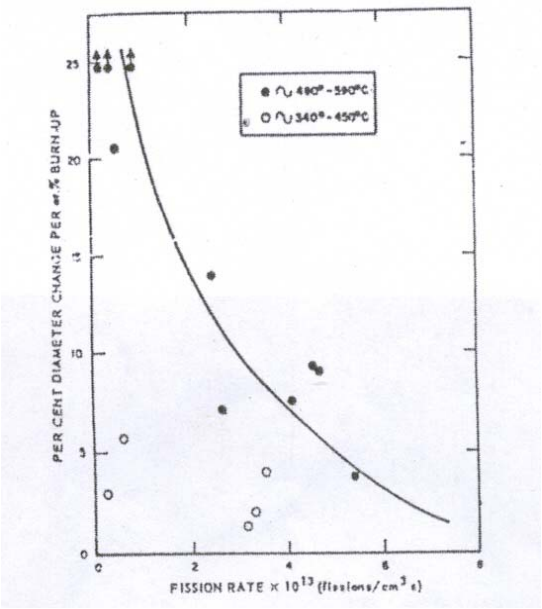

Fig. 3.6 Effect of fission rate on the swelling of U-10 wt.% Mo alloy rods, from Kittel et al. (Ref. 8). Range of RERTR tests: 2-6 x 10^{14} cm $^{-3}$ s^{-1}.

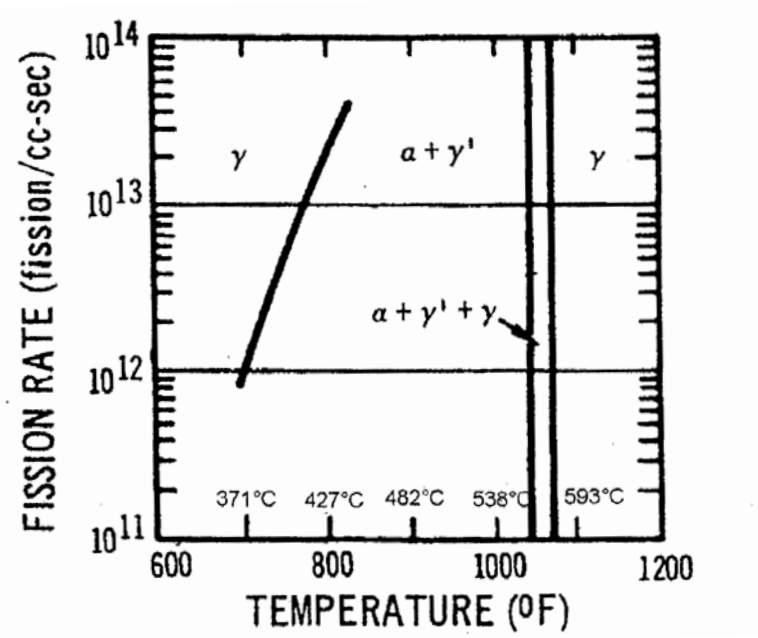

Fig. 3.7. Gamma stability of U-Mo alloy during irradiation.

Willard and Schmitt [9, 10] determined a critical fission rate – temperature correlation to demarcate the stable and unstable swelling regimes. Their results are given in Table 3.1 and Fig. 3.7.

Table 3.1. Calculated critical fission rate made using Eq. (3.1).

Temperature (K)	Critical Fission Rate (fissions/cm^3-sec)
644	8.8 x10^{11}
658	2.2 x10^{12}
672	4.8 x10^{12}
686	9.2 x10^{12}

The data are represented by the correlation

$$FR_{cr} = 3.75 \times 10^{28} \exp\left(-\frac{24{,}600}{T}\right) \quad \text{(f/cm}^3\text{-sec)} \tag{3.1}$$

3.4 References for Section 3

1. T.B. Massalski, Binary Alloy Phase Diagrams, ASM International, 1990.
2. P.E. Repas, R.H. Goodenow, R.F. Hehemann, "Transformation Characteristics of U-Mo and U-Mo-Ti Alloys," Trans. Amer. Soc. Metals, 57 150-63 (1964).
3. R.F. Hills, D.R. Harries, D.J. Hodkin, M.B. Waldron, "Transformation of Metastable Phases in the Uranium-Molybdenum Alloy System," AERE M/R 2840, U.K.A.E.A. Harwell (1959).
4. R.K. McGeary, "Development and Properties of Uranium-Base Alloys Resistant in High Temperature Water," USAEC Report WAPD-127, I. (1955).
5. R.J. Van Thyne, D.J. McPherson, "Transformation Kinetics of Uranium-Molybdenum Alloys," *Trans. ASM* 49 598-621 (1957).
6. Van Thyne, R. J., *Uranium Alloys Newsletter*, 13, November 1955.
7. G. Cabane, G. Donzé, "Stabilisation de la Phase γ dans les Alliages Ternaires à Base D'Uranium-Molybdene," *J. Nuc. Mat.* 4, 364-73 (1959).
8. J.H. Kittel and S.H. Paine, "Effect of Irradiation on Fuel Materials," in Proceedings of the Second United Nations International Conference on the Peaceful Uses of Atomic Energy, vol. 5, Basic Metallurgy and Fabrication of Fuels, 1-Sept. – 13 Sept., 1958, Geneva, Switzerland.
9. R.M. Willard and A.R. Schmitt, "Irradiation Swelling, Phase Reversion, and Intergranular Cracking of U-10 wt.% Mo Fuel Alloy," NAA-SR-8956 (February 1965).
10. J.L. Arnold, K.J. Miller, R.M. Peterson, "U-10 wt.% Mo Fuel Element Irradiation in SRE", NAA-SR-11121 (1965).

SECTION 4 DIFFUSION

4.1 Interdiffusion of Uranium in Molybdenum

The curve obtained from 800 to 1075°C for the U-UMo couple is characteristic of a single-phase diffusion. From the prepared curve the diffusion coefficients were calculated by the Matano method for each concentration, as shown in Fig. 4.1 [1]. As can be seen from this figure, the diffusion coefficient *D* varies widely with the U concentration. In the U-UMo system, because of the restricted concentration field, the variations in *D* with the U concentration are limited to one branch of the U-shape.

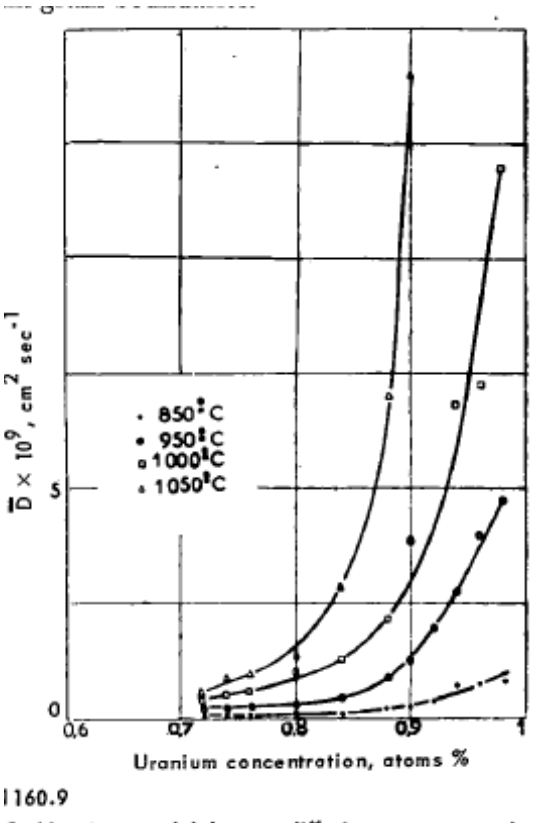

Fig. 4.1. Uranium-molybdenum diffusion; pure uranium and U-Mo alloy couple; diffusion coefficient as a function of concentration.

The curves for each concentration have been drawn, viz., log $D = f(1/T)$, T being the absolute temperature. Since curves are straight lines, Adda and Philibert [1] were able to determine the activation energy Q (Fig. 4.2) and the frequency factor D_0 corresponding to each concentration (Table 4.1)

Table 4.1. Uranium and Uranium-Molybdenum Alloy Diffusion

Uranium, at./at.	D, cm^2sec^{-1}				Q, kcal/g at.	D_0, cm^2sec^{-1}
	850°C	950°C	1000°C	1050°C		
0.74	8.9×10^{-11}	2.6×10^{-10}	5.5×10^{-10}	8.6×10^{-10}	34.0	2.1×10^{-4}
0.76	8.3×10^{-11}	2.6×10^{-10}	6.0×10^{-10}	1.1×10^{-9}	38.5	4.5×10^{-4}
0.80	9.9×10^{-11}	3.0×10^{-10}	1.1×10^{-9}	1.4×10^{-9}	39.4	3.0×10^{-3}
0.84	1.3×10^{-10}	4.8×10^{-10}	1.3×10^{-9}	2.9×10^{-9}	45.7	9.6×10^{-2}
0.88	2.0×10^{-10}	8.9×10^{-10}	2.3×10^{-9}	7.1×10^{-9}	52.2	3.2
0.90	2.6×10^{-10}	1.3×10^{-9}	3.2×10^{-9}	1.5×10^{-8}	56.8	28.0
0.92	4.0×10^{-10}	2.0×10^{-9}	5.7×10^{-9}	1.7×10^{-8}	55.0	16.0
0.94	6.9×10^{-10}	2.8×10^{-9}	6.9×10^{-9}	1.7×10^{-8}	53.0	20.0
0.96	6.2×10^{-10}	4.0×10^{-9}	7.4×10^{-9}	1.5×10^{-8}	45.8	5.8×10^{-1}
0.98	8.3×10^{-10}	4.8×10^{-9}	1.2×10^{-8}	1.7×10^{-8}	47.5	2.2

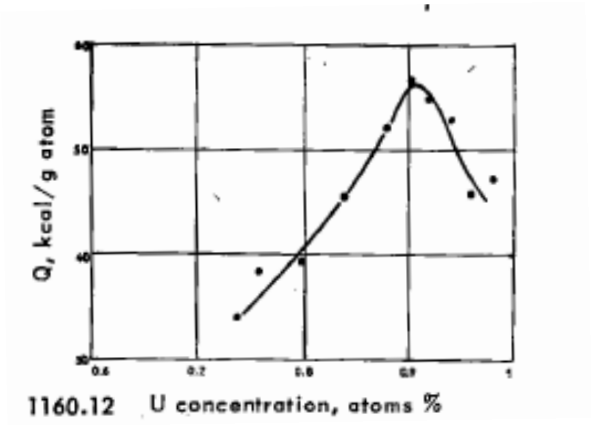

Fig. 4.2. Uranium-molybdenum diffusion; the energy of activation for chemical diffusion as a function of concentration[1].

4.2 References for Section 4

1. Adda, Y. and Philibert, J., "Diffusion of Uranium with some Transition Metals," in Proceedings of the Second United Nations International Conference on the Peaceful Uses of Atomic Energy, vol. 6, Basic Metallurgy and Fabrication of Fuels, 1-Sept. – 13 Sept., 1958, Geneva, Switzerland.

SECTION 5 MECHANICAL PROPERTIES

The mechanical properties of U-Mo have only a secondary impact on fuel behavior, through the effect that these properties have on U-Mo irradiation behavior. For the monolithic fuel, at least, the mechanical properties might be important for the overall plate properties. A brief summary is included here for completeness, and to aid in efforts to model fuel particle irradiation behavior. As is the case for aluminum alloys, U-Mo as typically used for research reactor fuel is in a non-equilibrium state, and the mechanical properties of U-Mo vary widely as a function of thermal history.

The majority of the material in this section was taken directly from Ref. 1.

5.1 Young's Modulus

Table 5.1 lists values for Young's modulus of various U-Mo alloys at room temperature[1].

Table 5.1. Young's modulus of the U-Mo alloys at room temperature[1].

Alloy	Property	E (MPa)
U-8Mo ingot	as-cast	50,500
	homogenized	50,860
U-10Mo ingot	as-cast	84,000
	homogenized	N/A
U-10Mo plate	as-cast	91,000
	homogenized	91,400
U-10Mo rolled	RW	83,000
	WR	88,000
U-12Mo ingot	as-cast	94,300
	homogenized	92,600

5.2 Hardness

A selection of hardness data for materials that have been 'γ-annealed' at 800° -900°C is presented here. Hardness data as a function of temperature from two sources [2-4] are presented in Table 5.2 and is plotted in Figs. 5.1a and 5.1b. Hardness tends to increase with molybdenum content in the range of 7-14 wt.%. Data shown in Fig. 5.1b show that in the composition range of 7.8 – 10.9 wt.% molybdenum, hardness differences are small but may be detectable given a sufficient number of measurements.

The change in hardness due to fission was measured by Bleiberg [3]. In general, the hardness was found to increase with irradiation up to the maximum tested burnup of 8800 MWD/t.

Table 5.2. Hardness and tensile properties of the alloys at room temperature [1].

			$\dot{\varepsilon} = 0.833 * 10^{-3} s^{-1}$					
	Property	Hardness (30kg)	σ_{y^0}	$\sigma_M = \sigma_{y^{0.2}}$	A	$\frac{S_0 - S_u}{S_0}$	Σ	E
Alloy		Hv	MPa	MPa	%	%	%	MPa
U-Mo 8 U 413 ingot	as-cast	257	837	908	14.3	15.4	22.7	50 500
	homogenized	258	770	833	7	11.4	23.6	58 600
U-Mo 10 D 422 ingot	as-cast	282	873	922	8	4.5	23	84 000
	homogenized	286	–	923	5.8	4	10.3	–
U-Mo 10 D 407 plate	as-cast	285	765	870	13.4	–	–	91 000
	homogenized	289	789	902	15.5	–	–	91 400
U-Mo 10 D 487 rolled	R W	283	734	953	15.3	13.5	32	83 000
	W R	283	659	955	11.1	12.3	29	88 000
U-Mo 12 N 146 ingot	as-cast	314	–	749 ($< \sigma_{y^0}$)	0	0	0	94 300
	homogenized	314	–	647 ($< \sigma_{y^0}$)	0	0	0	92 600

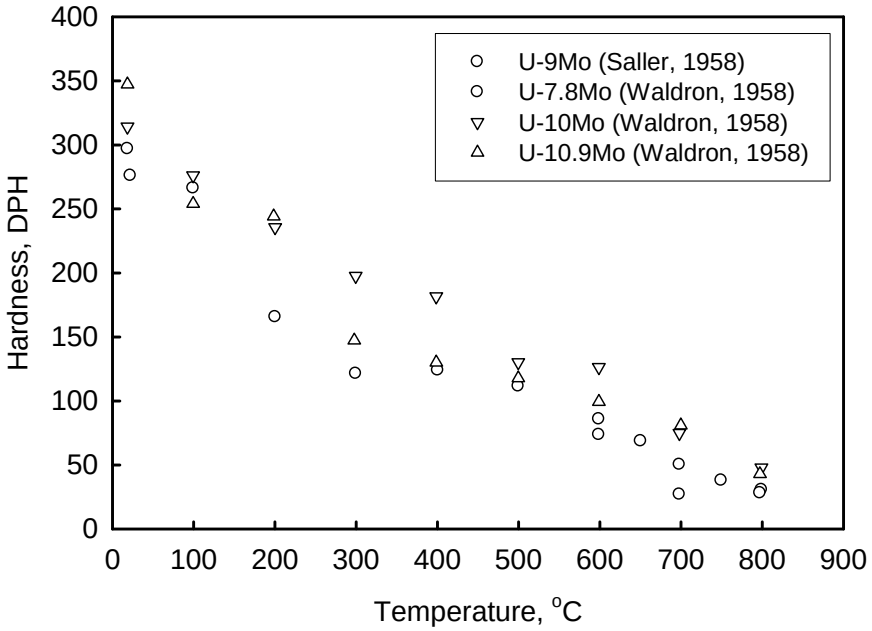

Figure 5.1a. Hardness data for γ-annealed U-Mo alloys.

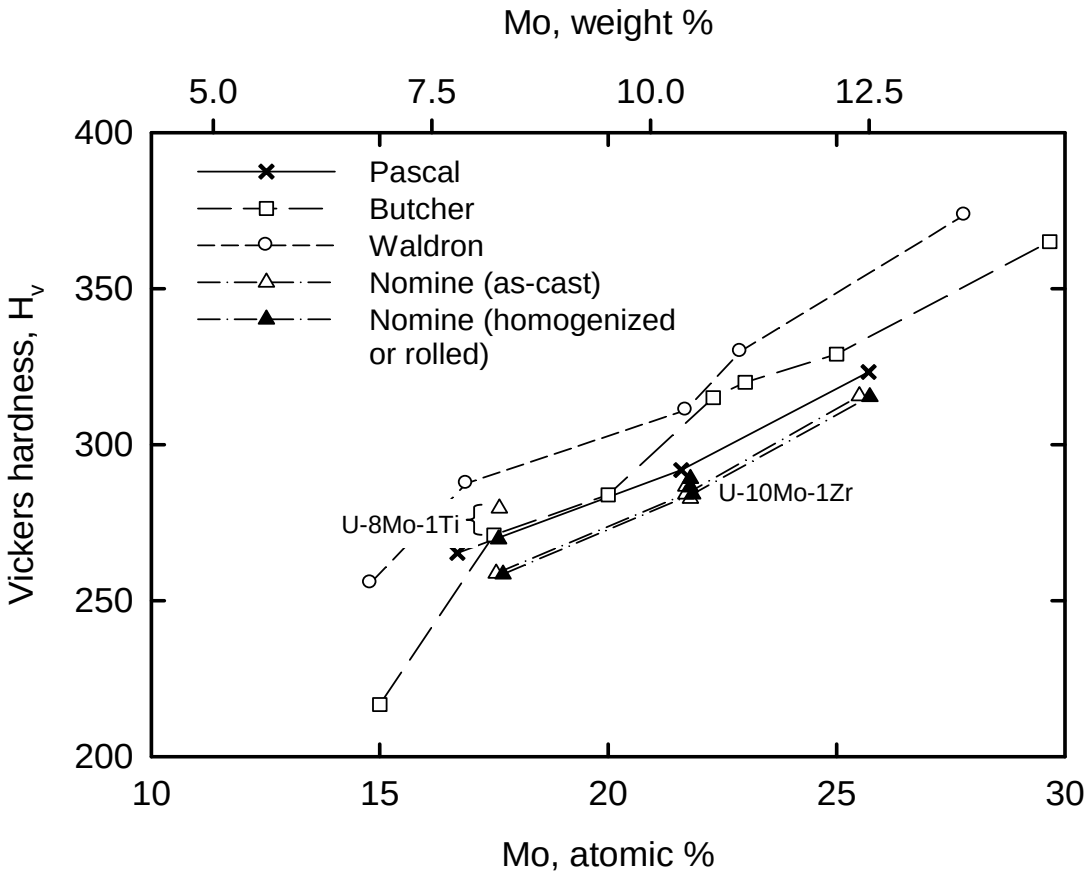

Fig. 5.1b. Variation in Vickers hardness with molybdenum content for the alloys[1,4-6].

5.3 Tensile and Compressive Properties of U-Mo Alloys

The maximum yield stress (Fig. 5.2) increases when the molybdenum content is increased from 8 to 10% (Table 5.2). Compression tests performed on the U-12Mo alloy at $0.96 \times 10^{-3} s^{-1}$ (Table 5.3) shows a maximum stress larger than that of the U-10Mo alloy [1]. These results are in keeping with Butcher [5] but not with Waldron [4].

The ductility (Fig.5.2) decreases when the weight fraction of molybdenum in the γ phase increases (approaching zero for the U-12Mo alloy): this drop in ductility was observed by Waldron [4] and, to a lesser extent by Butcher [5].

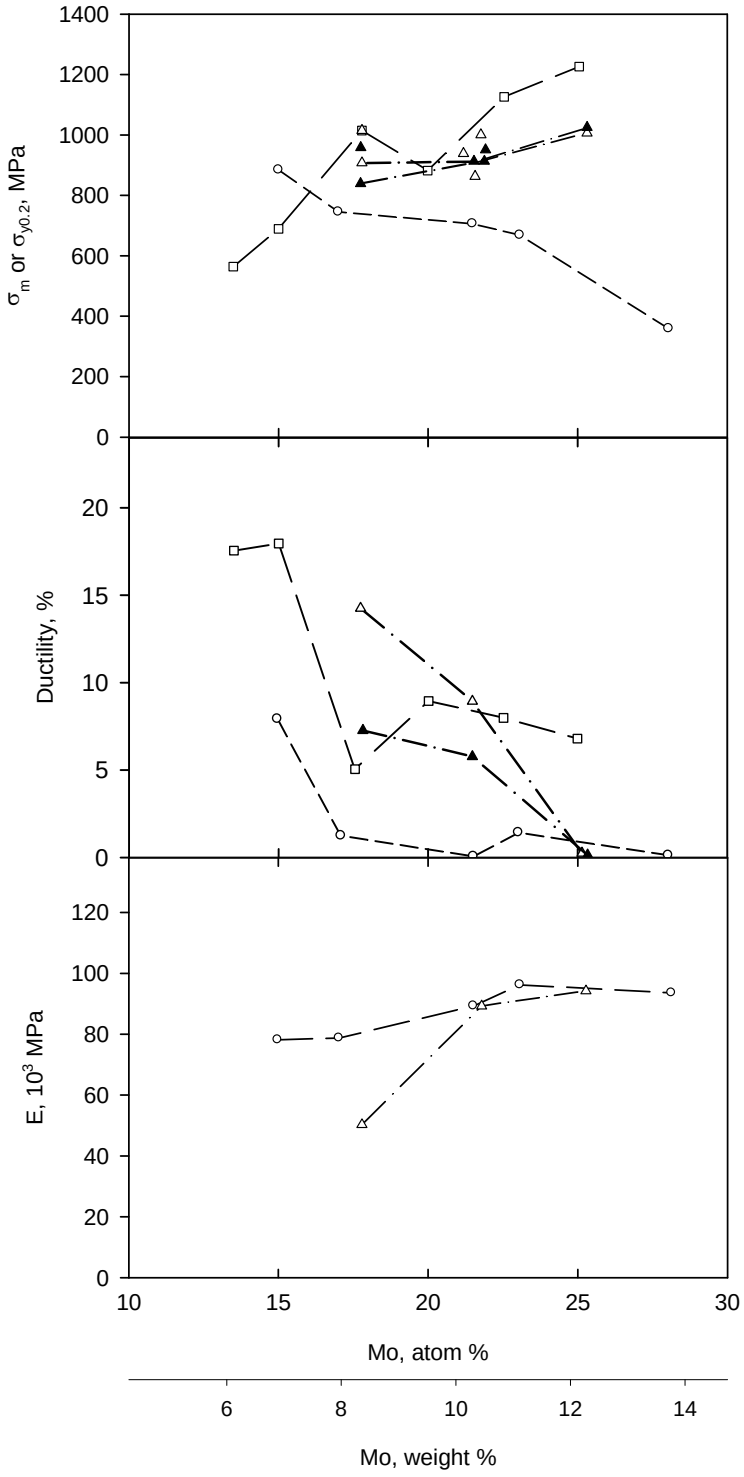

Fig. 5.2. Variation in tensile properties with molybdenum content for the alloys [1].

Table 5.3. Compressive properties of the U-12Mo alloy.

Alloy	Property	$\dot{\varepsilon} = 0.96 \times 10^{-3}\ s^{-1}$	
		σ_{y0} MPa	$\sigma_{y0.2}$ MPa
U-12Mo	As-cast	943	1015
N 146 ingot	Homogenized	951	1018

5.4 References for Section 5

1. Nomine, A. M., Bedere, D., and Miannay, D., "Grandeur, mecaniques associées à la corrosion sous contrainte de I'alliage U-10Mo," paper presented at the Coloque sur la rupture des materiaux, Grenoble, 9-21 January 1972.
2. Saller, H.A., Dickerson, R.F. and Hurr, W.E., Report BMI-1098 (1956)
3. Bleiberg, M.L., et al., Report WAPD-127, Part IV, Atomic Energy Commission (1957)
4. Waldron, M. B., Burnett, R. C., and Pugh, S. F., "Mechanical Properties of Uranium-Molybdenum Alloys," Atomic Energy Research Establishment, Harwell, England, Report No. AERE-M/R-2554, 1958.
5. Butcher, B.R., Hills, R. F., and Howlett, B. W., "The Mechanical Properties of Quenched Uranium-Molybdenum Alloys. Part I: Tensile Tests on Polycrystalline Specimens," J. Nucl. Mater., 11(1964), 149-62.

Intentionally Blank Page

SECTION 6 U-Mo IRRADIATION PERFORMANCE

6.1 U-Mo Swelling

Various data on irradiation swelling for U-Mo alloys are available in the literature [1-10]. Among them, only monolithic U-Mo data obtained at temperatures <600°C are used to extract swelling data. Data for U-Mo dispersion-type fuel have been excluded by the authors because the volume increase of the specimens caused by the formation of the fuel/matrix interaction layer is difficult to separate from that induced by fuel swelling.

The total swelling is composed of two elements: swelling due to solid fission products, and swelling due to gas-phase fission products. Swelling due to solid fission products is proportional to burnup; it is independent of temperature and alloying parameters, such as Mo content and fabrication processes. Therefore, this type of swelling is usually given by a linear function of burnup. However, swelling due to gas-phase fission products is in principle a thermally activated phenomenon. It depends on fuel temperature and Mo content as well as burnup.

The U-Mo swelling correlation is composed of two parts: solid fission product swelling and gas bubble swelling.

$$\left(\frac{\Delta V}{V_0}\right)_{total}(\%) = \left(\frac{\Delta V}{V_0}\right)_g + \left(\frac{\Delta V}{V_0}\right)_s \tag{6.1}$$

Solid swelling

The solid fission product swelling is a linear function of burnup (or fission density) [1].

$$\left(\frac{\Delta V}{V_0}\right)_s(\%) = 3.5\times10^{-21} f_d \tag{6.2}$$

where f_d is the fission density in fissions/cm^3.

Gas bubble swelling

The gas bubble swelling has different rates depending on the fission density.

$$\left(\frac{\Delta V}{V_0}\right)_g(\%) = 1.8\times10^{-21}(f_d), \quad \text{for } f_d \le 3\times10^{21} \text{ f/cm}^3, \tag{6.3}$$

$$\left(\frac{\Delta V}{V_0}\right)_g(\%) = 5.4 + 2.1\times10^{-21}\left(f_d - 3\times10^{21}\right) + 0.43\times10^{-42}\left(f_d - 3\times10^{21}\right)^2, \quad \text{for } 3\times10^{21} \le f_d. \tag{6.4}$$

where f_d is the fission density in f/cm^3.

A comparison between the measured data and correlation predictions is given in Fig. 6.1.

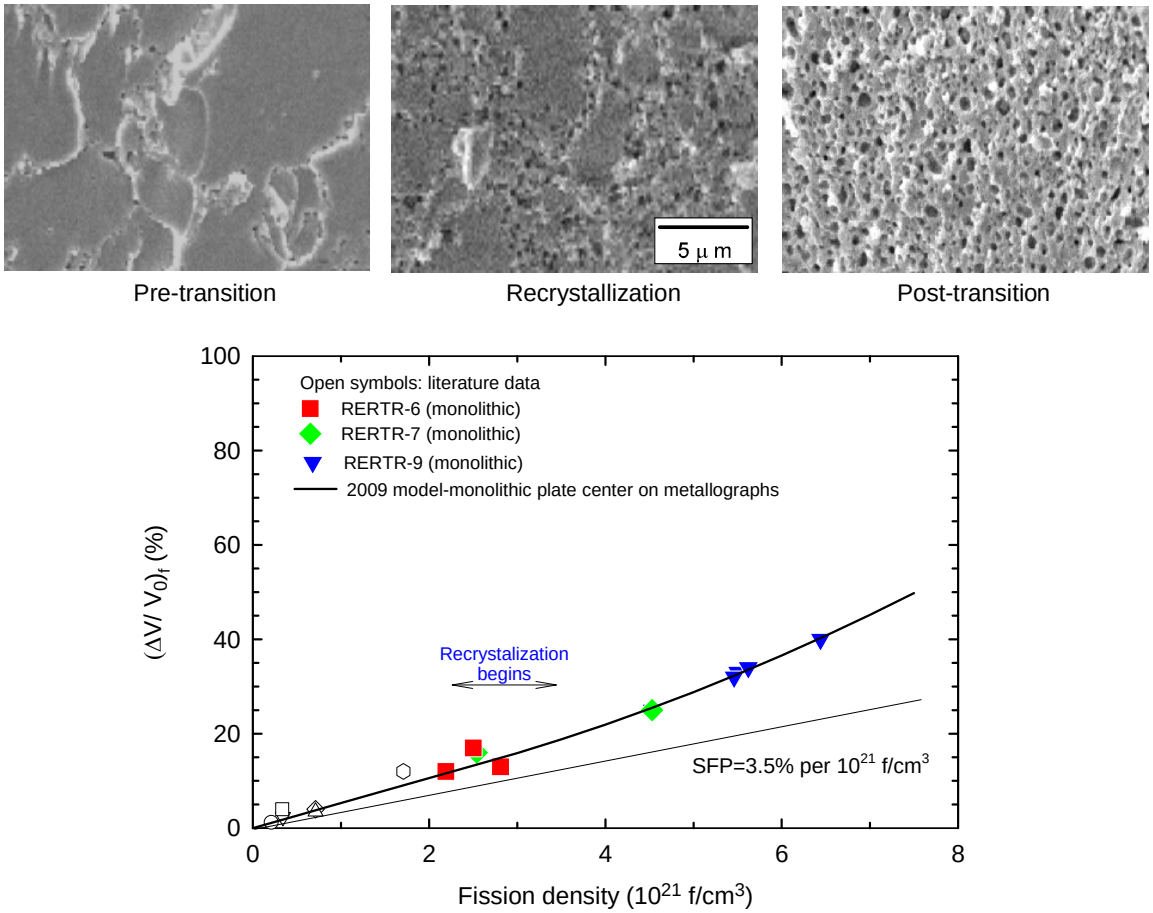

Fig. 6.1 Comparison of fuel swelling between measured data and correlation predictions.

An effect of the Mo content in the fuel alloy on swelling was also observed. The effect is shown for three Mo contents in Fig. 6.2. The explanation for the effect is still speculative and hence needs further analysis and study. Well characterized differences in the as-fabricated properties and microstructure would be helpful. As indicated in the graph, the scatter in the data is somewhat due to measurement, but mostly due to the difference in the burnup in the data because the swelling rate increases with burnup.

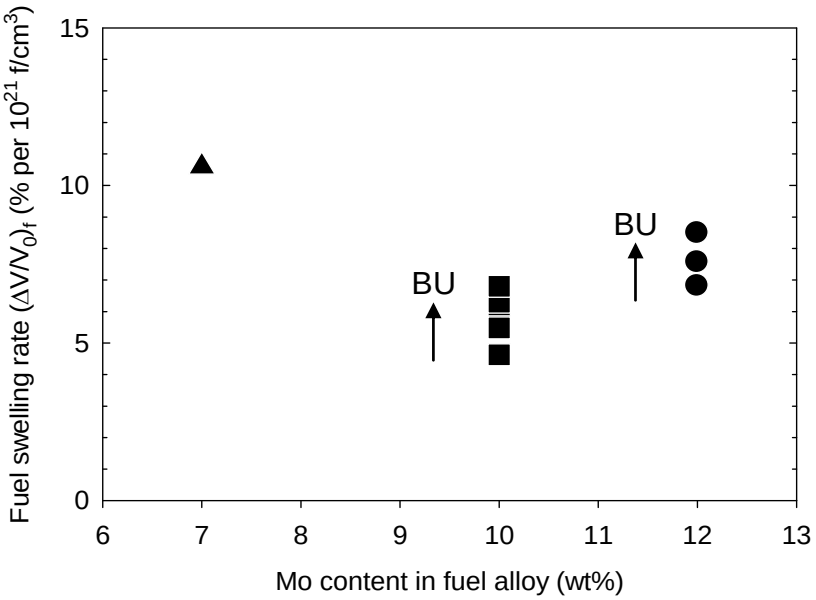

Fig. 6.2 Effect of the Mo content in fuel alloy on fuel swelling.

Notice that Eq. (6.1) is for the volume change based on the initial volume. The percent volume change based on the time-dependent volume is useful for other performance topics, such as the change in thermal conductivity with irradiation. $(\Delta V/V)_G$, is provided by

$$\left(\frac{\Delta V}{V}\right)_G = \frac{\left(\frac{\Delta V}{V_0}\right)_G}{1+\left(\frac{\Delta V}{V_0}\right)_G} \ . \tag{6.5}$$

Fig. 6.1 Burnup dependence of U-Mo swelling.

6.2 Change in U-Mo Thermal Conductivity during Irradiation

The thermal conductivity of U-Mo alloy decreases during irradiation due to the increase in porosity by gaseous swelling and buildup of fission products in the fuel. The impurity effect from solid fission products and the irradiation damage effect are not explicitly included in the modeling. Fission gas bubbles significantly change the thermal conductivity of the alloy. The thermal conductivity of fuel during irradiation is modeled by using the Bruggeman method [11, 12] considering the fuel as a composite of U-Mo metal and gas-filled pores. The fission gases are composed of Xe and Kr with a ratio of nine Xe atoms per one Kr atom.

The thermal conductivity during irradiation can be expressed as follows: using a two-phase model,

$$k_{U-Mo} = \frac{1}{4}\left[A + \left(A^2 + 8k^0_{U-Mo}k_g\right)^{\frac{1}{2}}\right] \tag{6.6}$$

where

$$A = (2 - 3P)k^{0}_{U-Mo} + (3P - 1)k_g \,, \tag{6.7}$$

$$P = \frac{1}{100}\left(\frac{\Delta V}{V}\right)_G \,. \tag{6.8}$$

Here k_{U-Mo} is in W·m^{-1}K^{-1}, k^{0}_{U-Mo} is the unirradiated U-Mo thermal conductivity given by Eq. (2.8) of Section 2, k_g is the pore thermal conductivity, P is porosity, and $\left(\frac{\Delta V}{V}\right)_G$ is gaseous swelling obtained in Eq. (6.5), above. The pore thermal conductivity filled with fission gases, assuming the Xe yield is nine times larger than the Kr yield, can be calculated using the data from MATPRO [13]:

$$k_g = 0.1\left(8.247\times10^{-5}\,T^{0.8363}\right) + 0.9\left(4.351\times10^{-5}\,T^{0.8616}\right) \tag{6.9}$$

where k_g is in W·m^{-1}K^{-1} and T is in K.

6.3 U-Mo Corrosion with Water in Defected Cladding

Information on corrosion of U-Mo alloy in water is available in Ref. 2. This section is a review of this report.

Although much of the data in the text of this report cannot be interpreted properly with respect to the effects of radiation on corrosion life because of improper specimen fabrication, certainly no evidence was found within the range of exposure used that would attest to the deterioration of γ-phase alloys. This conclusion was particularly borne out by the results of in-pile loop tests of defected clad samples of uranium molybdenum. Certainly the stabilizing effect of radiation on the γ phase would be expected to lengthen the life of these alloys. Indeed, samples which survived in-pile exposure to hot water for long periods failed on post-irradiation corrosion testing within very short periods. Incipient transformation of γ-phase alloys should influence corrosion behavior out-of-pile on long time exposure. In-pile, such transformations should be hindered by radiation; hence, corrosion life should be extended. An interesting corollary to this observation is that conducting development of corrosion resistant uranium-based alloys by out-of-pile testing may be impossible. The sensitivity of these alloys to radiation exposure is not unexpected. Experiments reported in WAPD-127, Part I, revealed that these alloys are quite tolerant to significant amounts of impurity contamination. Hence, deterioration of corrosion resistance by fission product contamination should not be severe. Likewise, lattice defect damage would be expected to have a second order effect on corrosion rates of materials that are controlled by formation of an external oxide.

Radiation induced no significant changes in the corrosion rates of γ-quenched U-Mo alloys in 343°C static water. However, radiation accelerated the failure of unclad samples; samples of U-12 w/o Mo water in 1 to 7 days, as compared with 66 days for unirradiated control samples. Clad γ-quenched U-Mo alloys irradiated to approximately 5000 MWD/t and defected after irradiation showed no significant changes in their corrosion lives. Clad samples of U-12Mo defected and irradiated in hot water loops successfully survived irradiation. Maximum exposures of 4000 MWD/t were reached for the U-12Mo alloys.

Table 6.1. Out-of-pile corrosion rates of non-irradiated and irradiated (γ-quenched) unclad U-Mo samples (Experiment 1B tested at 302°C, experiment 2B at 343°C).

Experiment No.	Sample No.	Composition	Heat Treatment	Exposure (MWD/T)	Ave. Corrosion Rate before Failure (mg/cm^2- hr)	Days to Failure
1B	30C	U-12 w/o Mo	Control	---	0.09	52-66
	80C		Control	---	0.11	45-52
	30H		6 wk, 200°C	---	0.07	49-56
	20H		6 wk,@300°C	---	0.07	49-56
	50H		6 wk,@400°C	---	0.04	49-56
	21H		6 wk @400°C	---	0.08	49-56
	11H		6 wk @500°C	---	---	0-1
	81		---	230	0.05	14-21
	40		---	650	0.05	7-14
	61		---	835	0.01	14-21
	8		---	1250	0.05	1-7
	0		---	1575	0.05	7-14
	51		---	1690	0.04	1-7
	90		---	2000	0.04	1-7
2B	6	U-10.5 w/o Mo	Control	---	0.24	21-35
	5		Control	---	0.25	21-35
	9		6 wk @ 200°C	---	0.28	7-14
	14		6 wk @ 300°C	---	0.23	14-28
	15		6 wk @ 400°C	---	1.3	7-14
	19		6 wk @ 500°C	---	---	0-1
	11		---	1050	0.30	22-28
	12		---	900	0.20	35-42
	13		---	445	0.26	22-28
2B	30	U-12 w/o Mo	Control	---	0.25	21-35
	29		Control	---	0.20	21-35

---: no irradiation

Table 6.2. Effect of irradiation on the corrosion resistance of transformed U-Mo alloys from post-irradiation tests (Experiment 6B: all samples tested in 343°C water at saturation pressure).

Specimen No.	Composition	Heat Treatment	Exposure (MWD/T)	Corrosion Rate after 24-hr test (mg/cm^2 hr)
A 3	U-9 w/o Mo	γ-Q + 200°C, 6 wk	---	-0.49
A 13	U-9 w/o Mo	525°C, 112 hr + 300°C, 6 wk	---	Disintegrated
A 6	U-9 w/o Mo	γ-Q	565	-0.32
A 8	U-9 w/o Mo	525°C, 112 hr	755	-9.00
A 9	U-9 w/o Mo	525°C, 112 hr	790	Broke into several pieces
B 8	U-10.5 w/o Mo	525°C, 112 hr + 300°C, 6 wk	---	Disintegrated
B 9	U-10.5 w/o Mo	525°C, 112 hr	730	-3.86
C 26	U-12 w/o Mo	525°C, 112 hr + 300°C, 6 wk	---	-3.59
C 23	U-12 w/o Mo	525°C, 112 hr	180	-2.83
D 23	U-13.5 w/o Mo	525°C, 112 hr + 300°C, 6 wk	---	-0.47
D 24	U-13.5 w/o Mo	525°C, 112 hr	170	-0.21

---: no irradiation

Table 6.3. Out-of-pile corrosion results of non-irradiated and irradiated clad U-10.5Mo samples (Experiment IC).

Sample No.	Heat Treatment	Exposure (MWD/T)	Days to Failure	Remarks
B 1	None after	920	45 - 57	Failure by splitting of clad near defect
B 2	extrusion	1020	23 - 32	Failure caused by corrosion of contaminated weld metal
B 3	"	1120	15 - 22	Failure caused by corrosion of contaminated weld metal
B 4	"	1090	15 - 22	Failure caused by corrosion of contaminated weld metal
B 7	"	950	45 - 57	Failure by splitting of clad near defect
B 8	"	630	8 - 14	Failure caused by corrosion of contaminated weld metal
B 9	"	810	45 - 57	Failure by splitting of clad near defect
B 10	"	630	45 - 57	Failure by splitting of clad near defect
BC 1	750°C for	None	45 - 57	Failure by splitting of clad near defect
BC 2	40 minutes	None	75 - 88	Failure by splitting of clad near defect
BC 3	"	"	75 - 88	Failure by splitting of clad near defect
BC 4	"	"	45 - 57	Failure by splitting of clad near defect
BC 5	"	"	23 - 32	Specimen bulged at defect
BC 6	None after	"	33 - 44	Failure by splitting of clad near defect
BC 7	extrusion	"	145 - 158	Failure by splitting of clad near defect
BC 8	"	"	33 - 44	Failure by splitting of clad near defect
BC 9	"	"	O.K. after	----------
BC 10	"	"	366 days	----------

Table 6.4. Post-irradiation corrosion life of irradiated clad U-Mo alloys (Pre-irradiation heat treatment: 750°C for ½ hr).

Sample No.	Composition	Exposure (MWD/T)	Test Days in 650°F Water to Failure
A 21	U-9 w/o Mo	3900	21 - 28
A 22		4930	14 - 21
A 23		5400	6 - 9
A 24		4410	14 - 21
A 25		7410	14 - 21
A 26		9335	3 - 6
A 27		9980	0 - 7
B 21	U-10.5 w/o Mo	3900	28 - 35
B 22		4930	35 - 42
B 23		5400	14 - 21
B 24		5100	26 - 33
B 25		4410	21 - 28
B 26		7410	15 - 16
B 27		9335	0 - 3
B 28		9980	0 - 7
C 21	U-12 w/o Mo	5610	6 - 9
C 22		5310	6 - 9
C 23		5610	14 - 21
C 24		5400	9 - 14
C 26		9550	0 - 3
C 27		10,490	0 - 3
C 28		9980	0 - 7
C 29		9335	0 - 7

Table 6.5. Out-of-pile corrosion life of unirradiated clad U-Mo alloys (Control samples for experiment 2C and 3C).

Sample No.	Composition	Heat Treatment	Test Days in 650°F Water to Failure
12-1	U-9.0 w/o Mo	750°C-1/2 hr	14 - 28
12-2		750°C-1/2 hr	14 - 28
12-3		750°C-1/2 hr	21 - 28
12-7		As-extruded	42 - 56
12-8		As-extruded	28 - 42
12-9		As-extruded	28 - 35
2-1	U-10.5 w/o Mo	750°C-1/2 hr	42 - 56
2-2		750°C-1/2 hr	56 - 70
2-3		750°C-1/2 hr	35 - 42
2-7		As-extruded	O.K. after 168 days
2-8		As-extruded	84 - 98
2-9		As-extruded	56 - 63
3-2	U-12.0 w/o Mo	750°C-1/2 hr	56 - 70
3-3		750°C-1/2 hr	42 - 56
3-4		750°C-1/2 hr	35 - 42
3-9		As-extruded	112 - 126
3-10		As-extruded	70 - 77
9-1	U-13.5 w/o Mo	750°C-1/2 hr	28 - 42
9-2		750°C-1/2 hr	28 - 42
9-3		750°C-1/2 hr	28 - 35
9-7		As-extruded	O.K. after 168 days
9-8		As-extruded	O,K. after 168 days
9-9		As-extruded	63 - 70

Table 6.6. In-pile test parameters for Chalk River loop test.

Specimen No.	Composition[5]	Enrichment (w/o U^{235})	Type of End Closure[1]	Diam. of Defect[2]	Calculated Exposure[3] (MWD/T)	Calc. Max. Temp. at Base of Defect[4] (°C)
M37	U-10.5 w/o Mo	3.6	Bonded	Not defected	1350	--
M39		3.6		Not defected	1145	--
M40		3.6		0.020 in.	1290	629
M41		3.6		0.012 in.	1510	647
M64		3.6		Not defected	1050	--
M65		3.6		Not defected	950	--
M67		3.6		0.007 in.	1510	647
M44		3.6	Unbonded	Not defected	1225	--
M45		3.6		0.008 in.	1430	641
M68		3.6		0.015 in.	1225	624
N35	U-12 w/o Mo	3.6		0.007 in.	1545	650
N36		3.6		Not defected	1290	--
N37		3.6		0.009 in.	1430	641
N41		3.6		Not defected	1050	--

Notes

(1) "Bonded" – end plugs pressure welded to core and clad. "Unbonded" – end plugs arc-welded to clad only.

(2) Defect drilled through clad with a 0.040 in. diam. drill.

(3) Exposure based on heat generation data from WAPD-CPM-1.

(4) Exposed to water for 6 weeks. Specimens at maximum temperatures approximately 2 days and at temperatures 30° lower for about 40 days.

(5) Fabrication history: All single melted in MgO crucibles. Poured into 1-1/4 in. ID copper molds at 1400°C. Extruded to 0.314 in. diam. at 1750° to 1950°F.

Table 6.7. Out-of-pile corrosion life of clad U-Mo alloys after irradiation in a hot water loop (Corrosion test conditions: 343°C static water at saturation pressure).

Specimen No.	Composition	Type of End Closure	Irradiation	Condition In-Pile	Exposure (MWD/T)	Days Failure
			Chalk River			
M 59	U-10.5 w/o Mo	Bonded	Hot Water Loop	Undefected	1145	7 - 14
M 64		Bonded			1050	14 - 21
M 65		Bonded			950	14 - 21
M 67		Bonded		Defected	1510	14 - 21
M 44		Unbonded		Undefected	1225	7 - 14
M 45		Unbonded		Defected	1430	14 - 21
M 68		Unbonded			1225	7 - 14
N 41	U-12 w/o Mo	Unbonded		Undefected	1050	14 - 21
M 60	U-10.5 w/o Mo	Bonded	MTR Process Water	Undefected	2730	28 - 35
M 58		Bonded			3620	35 - 44
M 59		Bonded			4720	28 - 35
M 63		Bonded			5040	O.K. after 58 days
M 61		Bonded			6730	O.K. after 58 days
M 62		Bonded			8580	O.K. after 58 days
M 43		Unbonded			2230	35 - 44
M 54		Unbonded			4030	O.K. after 58 days
M 53		Unbonded			4040	28 - 35
M 52		Unbonded			4460	21 - 28
M 56		Unbonded			7570	O.K. after 58 days
M 55		Unbonded			8160	O.K. after 58 days
N 38	U-12 w/o Mo	Unbonded			4970	28 - 35
N 40		Unbonded			8830	0 - 7
M 48	U-10.5 w/o Mo	Bonded	None	----	----	21 - 28
M 50		Bonded	None	----	----	28 - 35
M 51		**Unbonded**	**None**	**----**	**----**	**28 - 35**
N 34	**U-12 w/o Mo**	**Bonded**	**None**	**----**	**----**	**28 - 35**
N 47		**Unbonded**	**None**	**----**	**----**	**28 - 35**

Note: All samples were as-extruded. No heat treatment was given. Some un-irradiated test results are included for comparison (---: unirradiated).

Table 6.8. Out-of-pile corrosion life of clad U-Mo alloys after irradiation in the X-3 hot water loop (Corrosion test condition: 343°C static water at saturation pressure).

Specimen No.	Composition[2]	Irradiation[3]	Condition In-Pile	Exposure[1] (MWD/T)	Days to Failure
N50	U-12.1 w/o Mo	Chalk River	Undefected	2770	16 - 23
N51	U-12.1 w/o Mo	X-3 Hot Water Loop	Undefected	3060	0 - 9
N52	U-12.1 w/o Mo	X-3 Hot Water Loop	Undefected	3280	Not tested
N53	U-12.1 w/o Mo	"	Undefected	3420	16 - 23
N54	U-12.1 w/o Mo	"	Undefected	3520	0 - 9
N55	U-12.1 w/o Mo	"	Defected, 0.40 in. fuel exposed	3660	Not tested
N56	U-11.2 w/o Mo	"	Undefected	3630	16 - 23
N60	U-11.2 w/o Mo	"	Undefected	3630	0 - 9
N61	U-11.2 w/o Mo	"	Undefected	3520	16 - 23
N62	U-11.2 w/o Mo	"	Undefected	3420	0 - 9
N63	U-11.2 w/o Mo	"	Undefected	3280	Not tested
N64	U-11.2 w/o Mo	"	Undefected	3060	0 - 9
N65	U-11.2 w/o Mo	"	Undefected	2770	0 - 9
N70	U-12.1 w/o Mo	MTR Process Water	Undefected	2870	16 - 23
N71	U-12.1 w/o Mo	MTR Process Water	Undefected	4870	O.K. after 23 days
N72	U-11.2 w/o Mo	MTR Process Water	Undefected	6070	0 - 9
N73	U-11.2 w/o Mo	MTR Process Water	Undefected	6440	0 - 9
N74	U-11.2 w/o Mo	MTR Process Water	Undefected	6070	O.K. after 23 days
N75	U-11.2 w/o Mo	MTR Process Water	Undefected	5180	16 - 23
N76	U-11.2 w/o Mo	MTR Process Water	Undefected	3360	O.K. after 23 days
N49	U-11.2 w/o Mo	None	-	-	0 - 9
N49	U-12.1 w/o Mo	None	-	-	0 - 9

Notes

(1) Exposure of samples in Chalk River X-3 Loop based on heat generation data supplied by P. Frank. Exposure of samples in MTR Process Water based in maximum flux value and flux distribution supplied by MTR personnel.

(2) Fabrication conditions: all single melted in MgO crucibles. Poured into 1-1/4 in. ID copper molds at 1400^{o}C. Extruded to 0.314 in. diam. At 1750^{o} to 1950^{o}F.

(3) Irradiation time of samples in hot water loop:
Time in test -2365 hr
Time at 40 MW(full power) – 1803 hr
% time at 40 MW -76.2

6.4 References for Section 6

1. G.L. Hofman and M.K. Meyer, "Progress in Irradiation Performance of Experimental Uranium-molybdenum Dispersion Fuel," International Meeting on Reduced Enrichment for Research and Test Reactors, 2002.
2. M.L. Bleiberg, J.D. Eichenberg, R.H. Fillnow and L.J. Jones, Development and Properties of Uranium-base Alloys Corrosion Resistant in High Temperature Water, WAPD-127-Part IV, Westinghouse Electric Co., 1957.
3. D.O. Leeser, F.A. Rough and A.A. Bauer, in International Conf. on the Peaceful Uses of Atomic Energy, p.587, 1958.
4. R.S. Barnes, R.G. Bellamy, Butcher and P.G. Mardon, in International Conf. on the Peaceful Uses of Atomic Energy, p.218, 1964.
5. M.L. Bleiberg, L.J. Jones and B. Lustman, J. Appl. Phys., **27**, 1270, 1956.
6. G.W. Greenwood, J. Nucl. Mater., **6**, 26, 1962.
7. R.W. Willard and A.R. Schmitt, Irradiation Swelling, Phase Reversion, and Intergranular Cracking of U-10wt.% Mo Fuel Alloy, NAA-SR-8956, Atomics International, 1965.
8. B. Kryger, Contribution to the Study of Fission Gas Release in Metallic Nuclear Fuels, CEA-R-3888, 1969.
9. Yeon Soo Kim, G.L. Hofman, J. Rest, Y.S. Choo, A. Robinson, RERTR Meeting, 2009.
10. M.K. Meyer, G.L. Hofman, J.L. Snelgrove, et al., in Proc. of 1999 Int. Meeting on RERTR, Budapest, Hungary, Oct. 3-8, 1999.
11. Yeon Soo Kim and G.L. Hofman, AAA Fuels Handbook, Sect.A-6, Argonne National Laboratory, 2002.
12. D. A. G. Bruggeman, Annal. Physik., **24**, 636, 1935.
13. SCDAP/RELAP5/Mod 3.2 Code Manual, MATPRO-A Library of Materials Properties for Light-Water-Reactor Accident Analysis, NUREG/CR-6150, Vol. 4, Rev.1, INEL-96/0422, Idaho National Engineering and Environmental Laboratory, July, 1998.

Intentionally Blank Page

SECTION 7 ALUMINUM PROPERTIES

7.1 Density of Aluminum

The recommended value for the density of pure aluminum at room temperature is 2.70 g/cm^3.

7.2 Metallurgy of Aluminum Alloys

In order to understand the mechanical behavior of research reactor fuels, one must understand the metallurgy and properties of the aluminum alloys used in their construction. Aluminum alloys used for research reactor fuel plates are usually commercial materials selected on the basis of material properties adequate for the intended purpose. The most common of these are commercially pure aluminum powder, and aluminum alloys 6061, 1100, 8001, and the European AG3NE. Each number series, i.e., 6000, 1000, etc., used to describe the wrought product refers to a specific class of alloy compositions. Table 7.1 gives the classification and nominal compositions of common aluminum fuel alloys.

Table 7.1. Aluminum alloys commonly used in fuel plate fabrication.

Alloys Series	Classification	Major Alloy Constituents	Minor Alloy Constituents
1000	commercially pure aluminum, >99%		Si, Fe, Cu
5000	non heat treatable	Mg	Cr, Mn,
6000	Age-hardenable	Mg, Si	Mn, Cr, Cu
8000	Other alloying additions	Ni	
AG3NE	French cladding alloy similar to 5000 series		

Aluminum alloy 1100 is the standard commercially produced ‘pure’ aluminum alloy, and contains up to 1 wt.% of silicon and iron as impurities. These impurities are largely insoluble and contribute to the strength of the alloy. Pure aluminum has a tensile yield strength of about 10.4 MPa (1.5 ksi), whereas 1100 Al can have yield strength of up to 152 MPa (22 ksi). The alloy can be cold-worked to enhance its strength; strain hardened alloys are identified using an ‘H’ designation following the alloy designation. For example, 1100-H18 indicates a material in the full-hard condition.

Alloys in the 6000 series used for many applications in the U.S., belong to a class of age-hardenable alloys based on magnesium and silicon additions. These alloys depend on the ability of $MgSi_2$ to be alternately taken into solution and precipitated as a fine dispersion. Dispersion hardening in this way results in a marked increase in yield strength. Other minor alloying additions may also be made for specific purposes. Aluminum alloy 6061 is a medium strength alloy containing, in addition to magnesium and silicon, chromium and copper; chromium is added to increase strength and copper for grain size control.

The maximum solubility of $MgSi_2$ in Al is 1.85 wt.% at 595°C. By heating 6000 series alloys at a temperature in the range of approximately 520 – 560°C, the $MgSi_2$ precipitates that formed during prior processing are taken into solution in the aluminum. Various lower temperature heat treatments are then used to manipulate the reprecipitation morphology of the $MgSi_2$ and thus the material properties. The size and distribution of these precipitates controls the properties of the alloy; a fine dispersion of $MgSi_2$ is most desirable if the objective is to strengthen the alloy. The process whereby specific heat-treatments are used to manipulate alloy properties is called aging or age-hardening. Following the alloy designation, a temper designation that describes the alloy age-hardening process is often specified. The temper designation is separated from the alloy designation by a hyphen (e.g. 6161-O). Common designations are O for annealed and recrystallized material, which have the lowest strength but highest ductility, and T followed by another number (e.g. 6061-T6 or 6061-T651) for alloys that have been age hardened. A wide range of tempers are available. A few common age-hardening treatments for 6061 plate stock are 6061-T4, which designates an alloy that has been solution treated and subsequently aged at room temperature, and 6061-T6 for an alloy that had been solution treated and aged at 160°C for ~20 hours. Nominal properties of 6061 series alloys as a function of heat treatment are given in Table 7.2.

Table 7.2. Nominal tensile properties of 6061 alloys as a function of temperature.

Temp.	Description	Yield Strength MPa (psi)	Ultimate Tensile Strength MPa (psi)	Elongation (% in 5 cm)
O	annealed and recrystallized	(8000)	(18,000)	25
T4	solution treated and naturally aged	(21,000)	(35,000)	22
T6	solution treated and artificially aged	(40,000)	(45,000)	12
T81	solution treated, cold worked, and artificially aged	(52,000)	(55,000)	15
T91	solution treated, artificially aged, and cold worked	(57,000)	(59,000)	12

Heating the alloy at too high a temperature or holding at temperature for an excessive length of time results in coarsening of the precipitate phase and a subsequent decrease in material strength. Alloys in this condition are said to be ‘over aged’. It is thus important that the fabrication process be controlled to take into account the affects of thermal processing on alloy properties.

Al-Mg alloys are classified in the 5000 series. The commonly used French cladding material AG 3 NE falls into this category. Mg has a solubility in aluminum of up to 14.9 wt.% at 451°C, however, this falls to 3 wt.% at 200°C. The magnesium in most commercially available alloys is in solid solution and contributes to alloy strength through the solution hardening effect; this class of alloys is not effectively precipitation hardened. At higher Mg contents, above approximately 3.5 wt.%, Mg_2Al_3 can be precipitated, but often forms as a continuous grain

boundary phase, which is detrimental to mechanical properties and corrosion behavior. Due to impurity silicon, some $MgSi_2$ precipitates are typically present in commercial alloys.

7.3 Irradiation Behavior of Aluminum

In highly loaded dispersion fuels, the cladding is the major structural component of the fuel plate, and thus is the major load bearing component. It is therefore important to understand the evolution of material properties of the cladding alloys as a function of fluence and temperature.

Irradiation Swelling

As described above, the 6000 series of aluminum alloys is based on relatively minor additions of magnesium (0.6-1.2 wt.%) and silicon (0.4 – 1.3 wt.%). The magnesium and silicon additions allow for the possibility of dispersion-hardening upon heat treatment through the formation of fine precipitates of $MgSi_2$. An early study of the irradiation behavior of 6061 aluminum was conducted by McCoy and Weir [1]. An extensive compilation of property and behavior data for 6061 aluminum was conducted as part of the ANS (Advanced Neutron Source) program in the U.S.[2] An assessment of 6061-T6 aluminum for use as structural materials in this reactor was also conducted [3].

Swelling in aluminum occurs mainly due to the processes of void formation and transmutation of aluminum to silicon. Data for swelling of pure aluminum, 6061-T6, 1100-O, and 5052-O are shown in Fig. 7.1 [3] as a function of fast fluence at an irradiation temperature of 55°-65°C. Silicon (2.33 g/cm^3) that forms due to neutron capture is less dense than aluminum (2.70 g/cm^3) and so the transmutation reaction results in a net volume increase if silicon precipitates as the element. This is represented by the dashed line in Fig. 7.1. Swelling occurs at a rate of approximately 1 vol.% for every 6 wt.% of aluminum transmuted. In Al-Mg alloys (AG3NE, 5000 series), however, a net volume decrease is possible due to the formation of the $MgSi_2$ phase, which results in a net density increase. Volume increases above the dashed line in Fig. 7.1 are due to void swelling. Void swelling of pure aluminum at these temperatures is more than two orders of magnitude higher than that of 6061 and 5052 alloys, and approximately an order of magnitude higher than 'commercially pure' 1100-O. Void swelling is quite sensitive to irradiation temperature. At temperatures of greater than ~0.45 of the absolute melting temperature, self-annealing, or recombination of defects, occurs at a rapid rate, resulting in a void swelling rate near zero at 150°C.

Strength of Aluminum on Irradiation

McCoy and Weir [1] studied the tensile mechanical properties of 6061 aluminum in the O-temper, cold-worked, and T-6 conditions at several irradiation temperatures. Fast fluence was in the range of 0.4 – 2.8 x10^{23} m^{-2} (>2.9 MeV), with thermal fluence being approximately one order of magnitude higher. Postirradiation tensile tests were conducted at both room temperature and at the irradiation temperature. Data for room temperature yield strength are shown in Fig. 7.2 and elongation data in Fig. 7.3 for unirradiated and irradiated material in all three conditions. For irradiation temperatures above 115°C they found that within the scatter of the data, there were no apparent irradiation effects on mechanical properties at these relatively low fluences. For example, the strength gain resulting from cold-working was retained on irradiation at temperatures up to 150°C. Of interest is the fact that cold-worked materials retained their

strength at higher irradiation temperatures than the same alloy subject to an aging heat treatment (6061-T6).

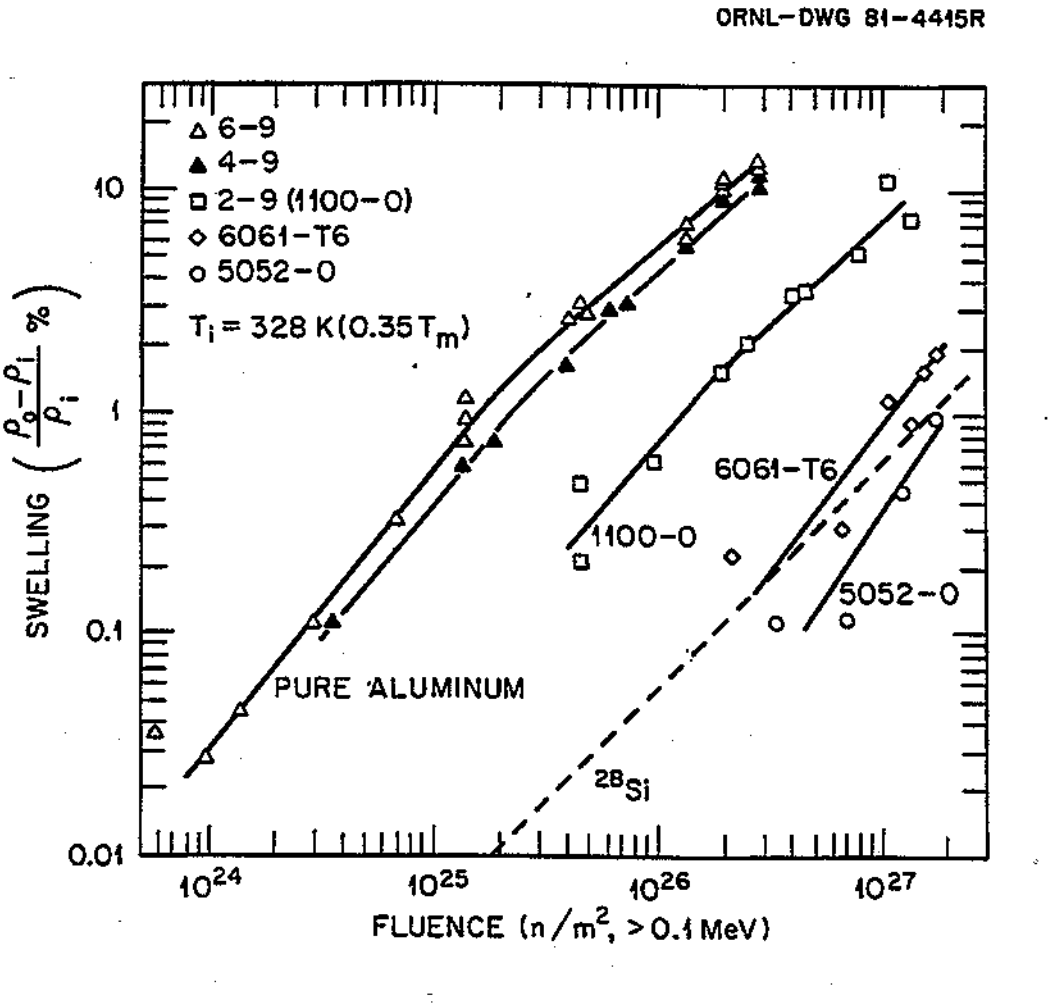

Fig. 7.1. Swelling behavior of aluminum during irradiation at 55°C.

Farrell has compiled data specific to 6061-T6 and 6061-T651 aluminum after neutron irradiation at temperatures less than 100°C to thermal neutron fluences of $5x10^{27}$ m^{-2}, considerably higher than those reported by McCoy and Weir. These data are shown plotted in Fig.7.4. Consistent with McCoy and Weir, little change in mechanical properties occurs until specimens reach a (thermal) fluence beyond ~5 x 10^{24} m^{-2} at which time significant strengthening occurs. This strengthening is presumably accompanied by a concomitant loss of ductility. Although the data scatter in the elongation plot in the lower part of Fig.7.4 is considerable, it appears that elongation does not fall below 3-4% at the highest fluence tested.

Fuel plate cladding temperature depends on the specific power and flow conditions at which the plate operates. Fuel plate cladding temperatures also depends strongly on the thickness of the surface corrosion layer. The formation rate of this layer varies widely depending on reactor water chemistry and the presence or absence of a fuel plate pre-filming regimen prior to reactor insertion (see Section 7.4).

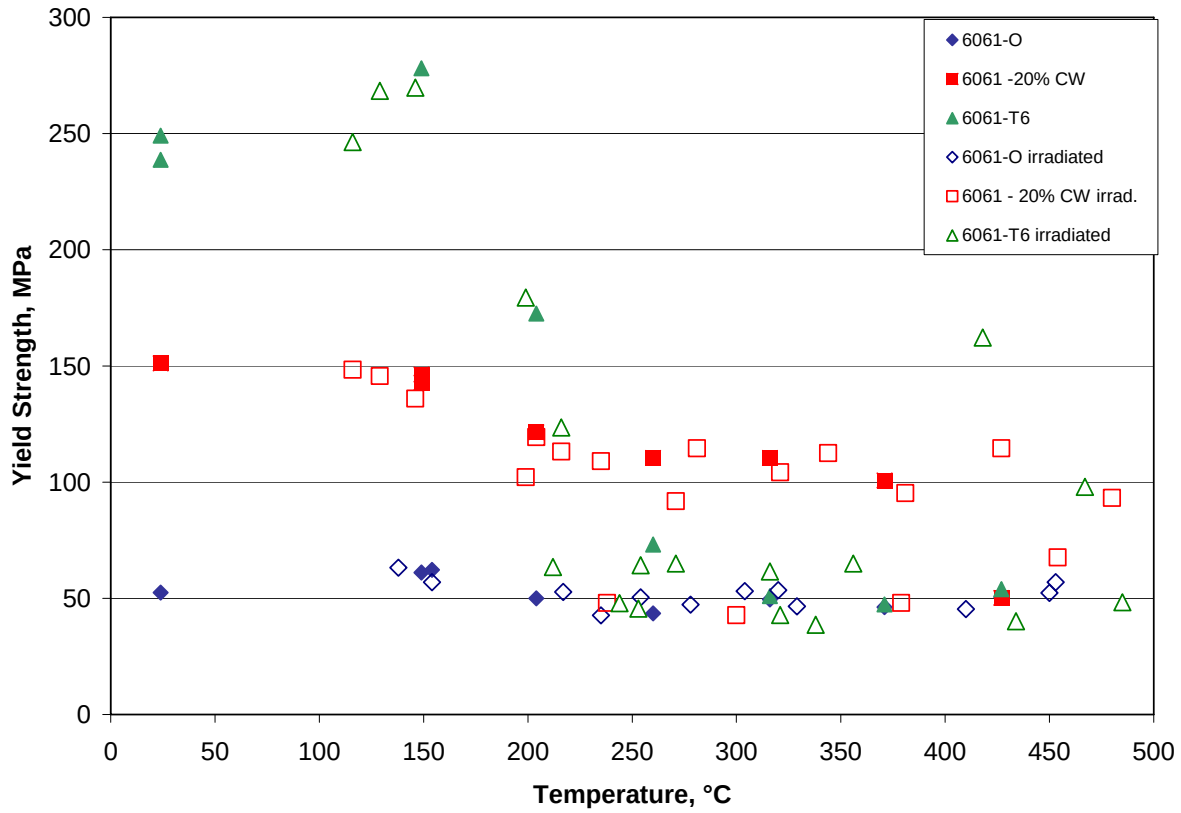

Fig. 7.2. Tensile yield stress (0.2% offset) of 6061 aluminum in the irradiated and unirradiated condition. 6061-O, 6061 with 20% cold work, and 6061-T6 conditions shown. Fast fluence was in the range of 0.4 – 2.8 x10^{23} m^{-2} (>2.9 MeV), with thermal fluence being approximately one order of magnitude higher.

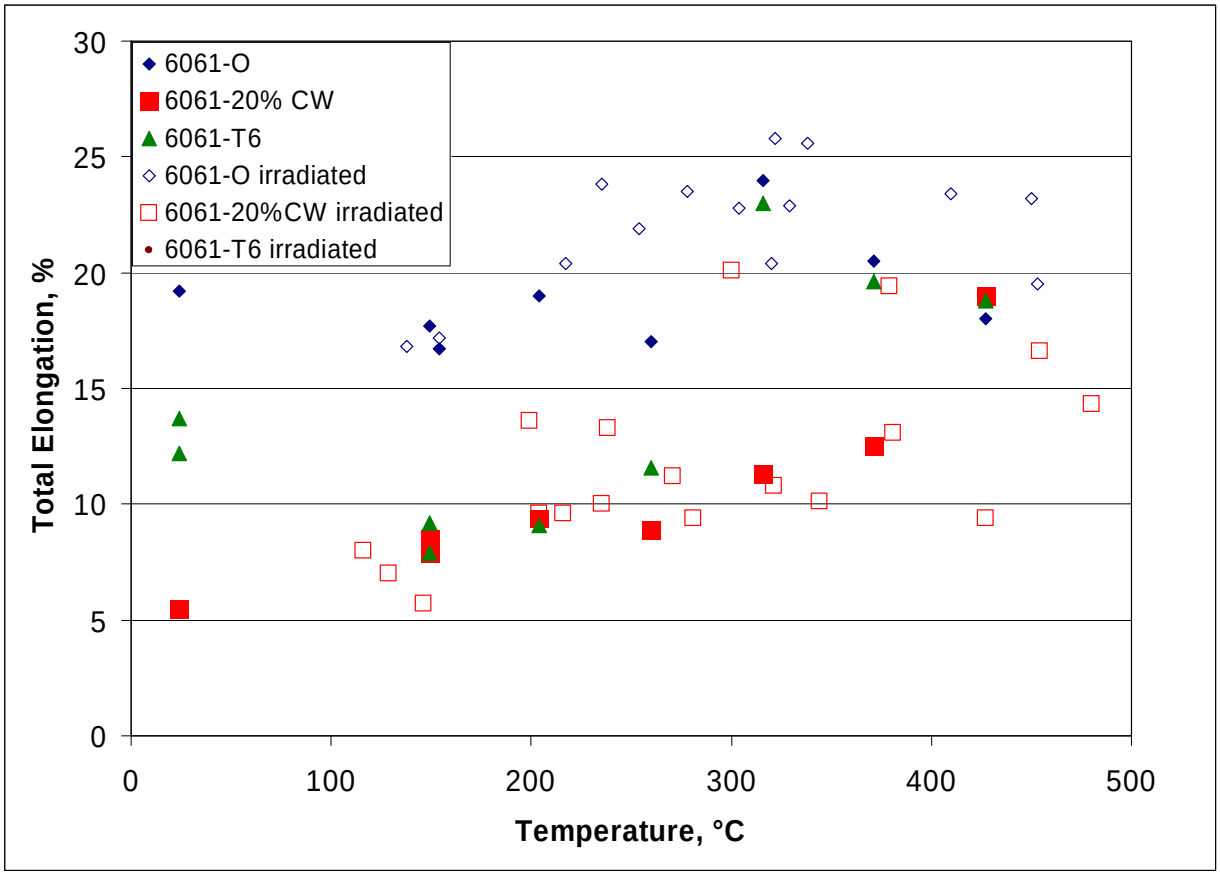

Fig. 7.3. Total elongation of 6061 aluminum in the irradiated and unirradiated condition. 6061-O, 6061 with 20% cold work, and 6061-T6 conditions shown. Fast fluence was in the range of 0.4 – 2.8 x10^{23} m^{-2} (>2.9 MeV), with thermal fluence being approximately one order of magnitude higher.

Hardness Change of Aluminum on Irradiation

Hardness measurement presents a convenient method for indirectly gauging the irradiation and thermal history of fuel cladding. The most common method of hardness testing on irradiated fuel is to use a microhardness tester to record DPH (Diamond Pyramid Hardness, or Vicker's hardness) at spacings as close as 25 μm. In this way, hardness can be plotted as a function of distance within thin fuel plates and cladding. Hardness data for commercial aluminum alloys are often reported as a macroscopic value on the Rockwell 'B' (HB) scale, and does not directly convert to DPH. Hardness also varies widely with material heat treat condition and the amount of cold work introduced during fabrication. The best practice for using hardness data as a tool for postirradiation evaluation is thus to collect out-of-pile data on archive material for direct comparison to postirradiation measurements on irradiated plates.

Hardness changes tend to trend with yield strength as a function of neutron exposure and temperature. The change in hardness on postirradiation annealing of 6063 aluminum is shown in

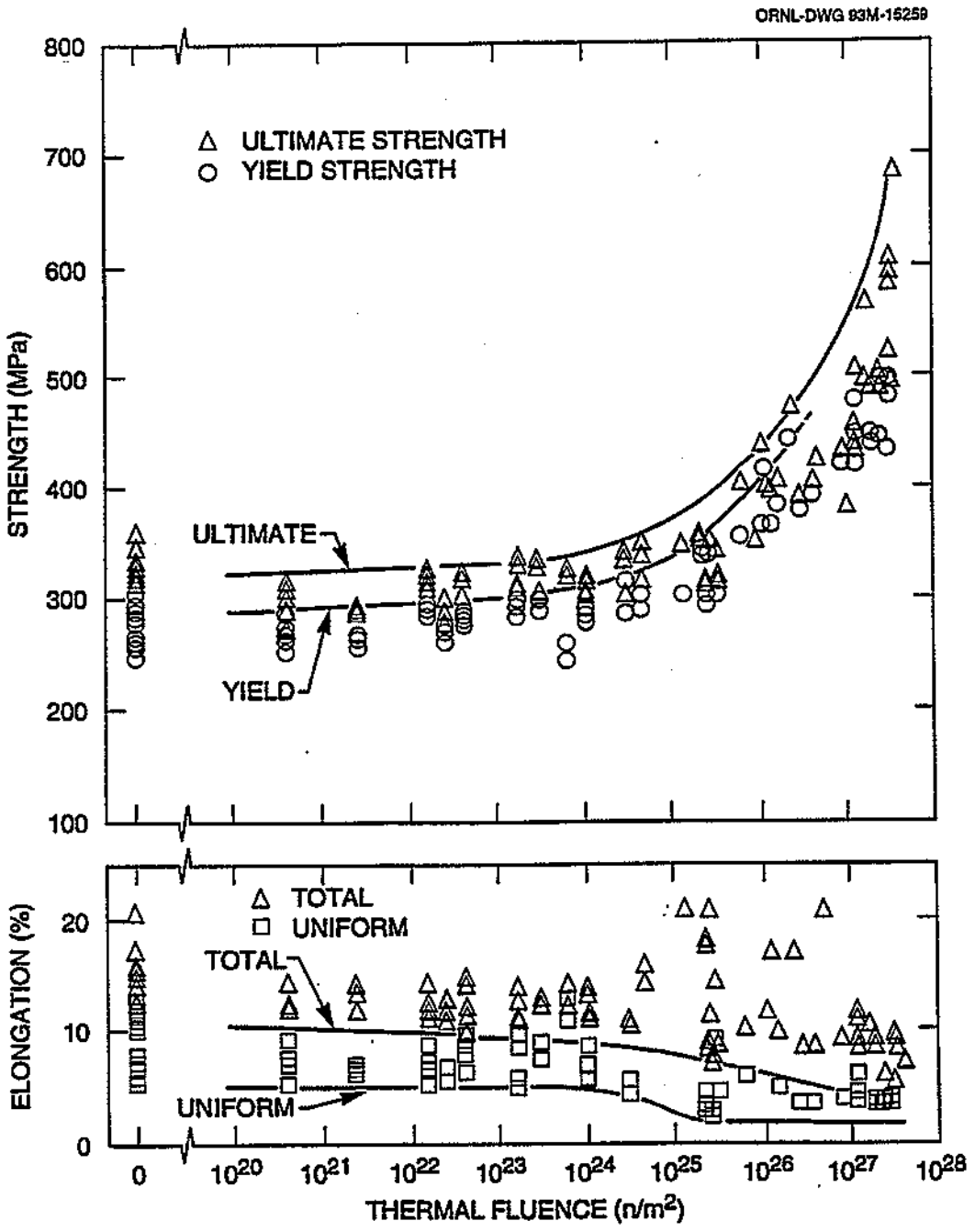

Fig. 7.4. Strength of aluminum alloys 6061-T6 and 6061-T651 after irradiation to the indicated thermal fluence at T<100°C.

Fig. 7.5. These data indicate that for cladding temperatures of 110°C, annealing of irradiation-induced hardening will not occur over times of 500 hours. At a temperature of 140°C, hardness decreases slowly as a function of time. At temperatures of 266°C, however, significant softening occurs within the first 10 hours of exposure to this temperature, and the hardness decreases to the same value as that of unirradiated material subjected to the same thermal anneal. This indicates that all effects of irradiation hardness have been removed by annealing at this temperature. It is

thus expected that 6063 irradiated at temperatures of 100°C would exhibit considerable irradiation induced hardening, while material irradiated at 260°C would exhibit a decrease in hardness.

As an example of the application of hardness data to the understanding of fuel plate performance, postirradiation hardness data from a few fuel plate irradiation experiments have recently been compared as a function of (calculated) temperature; these data are shown in Fig. 7.6 [4]. These data show that for cladding irradiated at temperatures less than 160°C, hardening occurs as expected. The data labeled UMUS is from a CEA fuel plate that that showed a considerable decrease in hardness during irradiation, indicating that the plate operated at a higher than expected temperature. The high cladding temperature was due to the formation of a thick surface corrosion layer.

As would be expected, fission recoil damage also results in changes in mechanical properties. The change in hardness of matrix aluminum was measured by Walker et al. [5] for UAl_3, U_3O_8, and niobium-coated U_3O_8 dispersion.. The Nb-coated U_3O_8 plates exhibit little change in hardness due to 'shielding' of the matrix from fission fragments by Nb. The U_3O_8 plates have lower fuel particle volume loading than the UAl_3 plates, and thus a smaller fraction of the matrix is exposed to fission fragment damage. This results in higher hardness for the UAl_3 plate matrix.

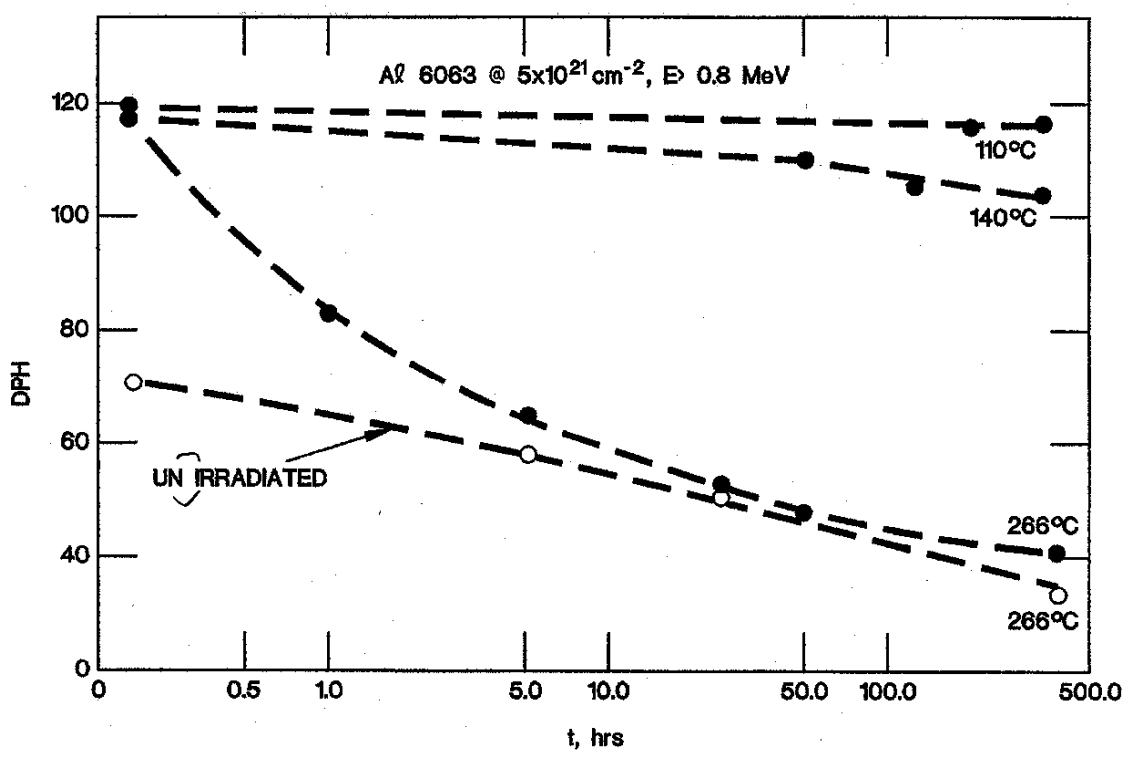

Fig. 7.5. Hardness change of irradiated 6063 aluminum as a function of postirradiation annealing time at three annealing temperatures. Also shown are data for unirradiated 6063 Al.

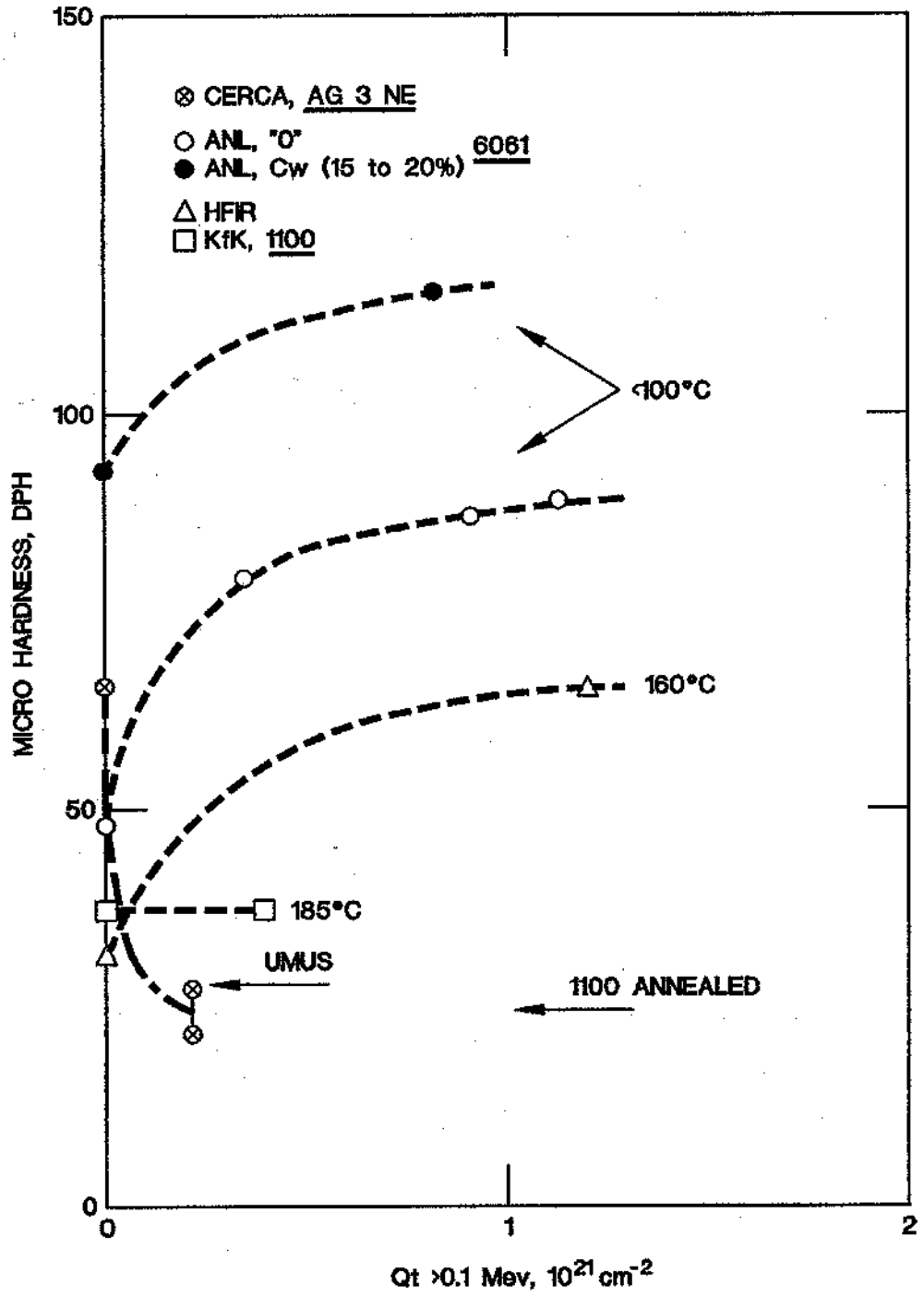

Fig. 7.6. Cladding hardness data as a function of fast fluence for irradaited fuel plates.

7.4 Aluminum cladding corrosion

Theory

The majority of the material in this section was taken directly from Ref. 6.

At temperatures below 400°C in air or water, aluminum will form one of several hydroxides on exposed surfaces. When the temperature of formation is below ~77°C, the end product will be a tri-hydroxide with the structure of Gibbsite (hydrargillite) [γ-Al(OH)3], if the pH is lower than ~5.8 or higher than ~9; Bayerite [α-Al(OH)3], if the pH is between ~5.8 and ~9; or Nordstandite [Al(OH)3], often considered a mixture of the other forms. When the temperature is above ~77°C and below ~102°C, a pseudoboehmite structure is formed, which may age to other hydroxide forms or retain its pseudoboehmite structure. Between ~102°C and ~400°C and at pressures below ~20 MPa (2900 psi), crystalline boehmite [γ-AlOOH] will form.

The technical understanding of how aluminum hydroxides form has improved greatly over the last 50 years. In water, these hydroxides are now known to form from precipitation and aging of gelatinous compounds of low crystal order and up to five moles of water per mole of oxide. Formation in water and from dilute acidic solutions is particularly important for understanding and predicting reactor fuel behavior.

The primary ionic species formed is [Al(H2O)6]3+, which provides the building block for octahedral chain molecules or hexagonal ring polynuclear complexes. Deprotonation and condensation reactions form a gelatinous boehmite that is the chemical precursor to both the tri-hydroxide and mono-hydroxide crystalline structures [7] (see Fig.7.7). Octahedral chain molecules, polynuclear complexes and the gelatinous boehmite structures need to be avoided within operating reactor nuclear fuel because their low-density structures are capable of blocking the annulus between fuel plates. Avoiding these chemical complexes in reactor service is achieved by preparing the fuel with the most appropriate hydroxide surface prior to usage and preventing the dissolution of that hydroxide during operation.

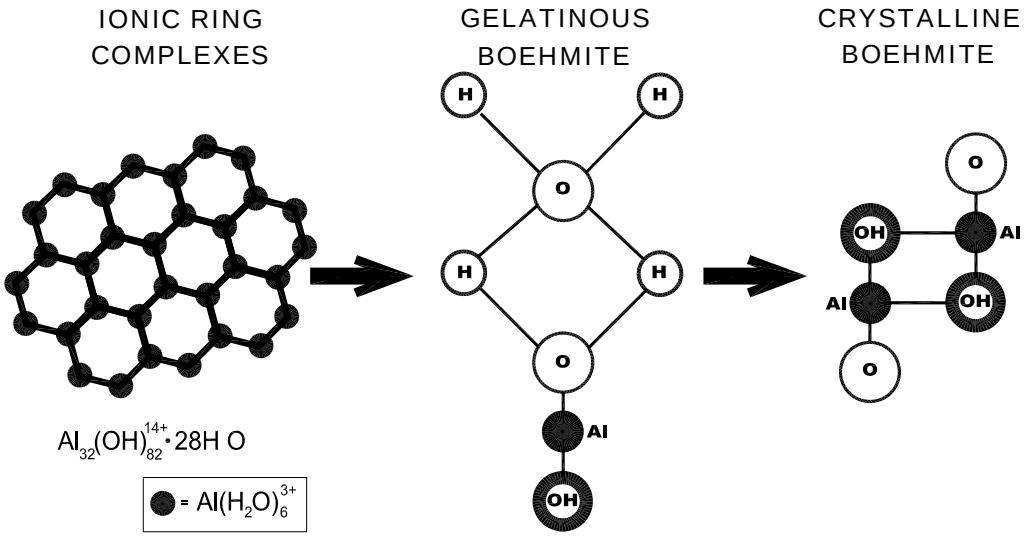

Fig. 7.7. Precipitation and aging of Al hydroxide to boehmite.

Aluminum hydroxides are amphoteric but relatively stable over a specific range of pH, primarily because of passivation due to the positive charge on the hydroxide surface provided by the Al3+ ion. The tri-hydroxide forms have a wider range of chemical stability (pH of ~ 4.0 – 8.5) but do not provide exceptional corrosion resistance within the region of passivation. Crystalline boehmite (mono-hydroxide) has a narrower passivation range (pH of ~ 4.7 – 6.2) but better water corrosion resistance within its range of stability. Boehmite treatments are commonly applied to improve the corrosion resistance of anodized aluminum components by "sealing" them in boiling water. Crystalline boehmite is routinely applied to Advanced Test Reactor fuel assemblies prior to their usage by treating them with deionized water in a high-temperature autoclave.

Acidic anions, especially carbonate and sulfate, have been shown to adversely affect the aging of alumina gels to achieve stable crystalline compounds. Chloride and nitrate are also undesirable but somewhat less damaging. Carbonate appears to have the strongest retarding effect. Conversely, removal of acidic anions from the chemical system helps accelerate the aging process. Because of these interactions, it is important that water supplies and water treatment systems prevent contamination with CO_2, carbonic acid, oxalic acid, or sulfuric acid.

Anodizing is an electrolytic method of depositing nearly pure Al_2O_3 on an aluminum surface. The metal is used as the anode in an electrolytic cell in an acidic electrolyte with a current applied to drive the chemical reaction with oxygen. Two basic types of anodizing treatments are in common use: those designed to provide a non-porous barrier oxide film, and those that generate a thick but porous structurally favorable coating. Porous anodic oxides are not discussed further as they could not perform the desired function. Barrier layer anodizing, however, could be used as an aluminum surface treatment. It could provide significant advantages over hydroxide coatings in that a very stable, fully crystalline alumina is generated. Barrier layer anodizing involves an electrolyte of either ammonium tartrate or boric acid and an operating voltage of typically 200 – 300V to generate an Al2O3 layer of up to 0.2 μm thickness. The layer formed is relatively pure Al2O3 but it will contain up to one percent of the acidic ion used in its formation. Boric acid electrolytes would be unacceptable for nuclear fuel. Although technically attractive, this approach to pretreatment does not have an existing experience base for use with nuclear fuel and would require testing for qualification before it could be seriously considered as a pre-treatment approach.

Corrosion is essentially an electrochemical process that may be enhanced by mechanical interactions or stresses on the components involved. Since aluminum is protected by a "corrosion" product, the term corrosion used here is defined as uncontrolled or unexpected hydroxide growth or change. Corrosion rates may be altered significantly (either positively or negatively) as a result of combinations of dissimilar metals or the application of electric currents. Conversely, corrosion can generally be minimized by maintaining water purity and preventing interactions with dissimilar materials in the reactor. The corrosion issues experienced with aluminum research reactor fuels are radiolysis and localized corrosion.

Neutron radiolysis is currently thought to cause breakdown of water molecules in the reactor coolant by ionization of the water to yield H_2O+, radical-cations, fast electrons, and electronically excited water molecules. The fast electrons rapidly thermalize and are solvated by interaction with neighboring water molecules to form what is chemically an anion of the hydrogen radical. This anion is the strongest known reducing species with a reduction potential

of –2.9V at a pH of 7. As a result, the anion rapidly grabs oxygen (from the water or from the aluminum hydroxide surface) to form O_2- that is a strong oxidizing agent and the precursor for formation of H_2O_2. The H_2O+ ions also decompose rapidly to form the OH- radical that may recombine as H_2O, H_2O_2, or HO_2. Radiolysis reactions are typically at a maximum near the surface of active fuel plates. The first few atom layers of water molecules next to the surface are affected both because of their proximity to the fission reaction and because of the nearly nonexistent flow rate of the water at the surface of the fuel. Radiolysis reactions cannot be avoided on nuclear fuel cladding surfaces. The radiolysis reaction, however, may either accelerate corrosion by facilitating the cathodic process or reduce the corrosion by anodic passivation [8].

Localized corrosion may occur in locations where water stagnates or is allowed to concentrate through evaporation such that its oxygen potential decreases and its ionic activity and acidity can increase beyond the hydroxide passivation range allowing the aluminum and/or its hydroxides to be attacked or dissolved. Localized corrosion includes pitting, galvanic, filiform, and crevice corrosive attack and often more than one specific mechanism is involved with corrosion issues. Although bulk reactor core water is normally quite clean, water that stagnates in corners, crevices, connector boxes, (or water that pools in such locations when the core is drained) may tend to increase in conductivity to the point that it becomes an effective electrolyte, allowing the corrosion mechanism to kick in. Localized corrosion is always exacerbated by galvanic interaction where dissimilar metals are in electrical contact and the electrical potential difference between the materials helps strip the positive charge from the anode and drive the corrosion reaction. Probably the most common situation with aluminum-clad fuels is contact with stainless steel components or reactor hardware. The difference in electro-negativity between the two metals promotes current flow leading to Al corrosion. The galvanic coupling of aluminum and stainless steel has been an especially difficult issue for spent fuel in water basins.

Most fuel cladding materials are active metals (Al, Zr, Mg, Cr, or Ni) where the cladding metal is protected from water corrosion by a stable passive surface compound containing oxygen. Radiolytic decomposition of surface oxides or hydroxides tends to be countered by reformation reactions that rebuild the surface protective layer. Therefore, the measurable effects of radiolysis may be very small if the cladding material rebuilds a structurally equivalent passive surface layer in rapid response to the radiolytic reactions taking place. This happens with Zr alloy commercial nuclear fuel cladding where core conditions are quite similar to the autoclave pre-filming conditions initially used to form the protective oxide. The Zr will continually re-form surface oxides damaged or lost during reactor operation. Although similar in principle, the re-formation of Al hydroxides is subject to the thermal limitations involved with specific Al hydroxides as matched with the reactor operating parameters. For example, the ATR reactor uses Al fuel protected with an autoclaved crystalline boehmite surface. Although the core water average temperature is only about 68°C the surface temperature of the fuel is considerably higher and is sufficient to form at least a pseudoboehmite structure when/if the hydroxide is damaged by radiolysis. For research reactor operations, where the average core water outlet temperature is around 38°C, the hydroxide resulting from reformation reactions would be difficult to predict without detailed data on the surface temperature and heat flux history for the fuel involved.

Corrosion during irradiation: RERTR test results

As described in detail in the preceding sections, a general feature in water-cooled reactors is the formation of corrosion products on the fuel cladding surface. The primary detrimental property of aluminum hydroxide is its low thermal conductivity, approximately one tenth that of the A1 cladding. It is a thermal barrier to the heat flow from the cladding to the water and causes the cladding and fuel meat temperature to increase. Corrosion does not present operational problems for typical low and medium power research reactors using fuels without pretreatment. As shown in Fig. 7.8 for fuel plates irradiated in the 30-MW Oak Ridge Research Reactor, the corrosion layers are uniform, adherent, and about 20 μm thick, for two Al-Mg cladding alloys used by European manufactures and the standard Al 6061 alloy used in the US.

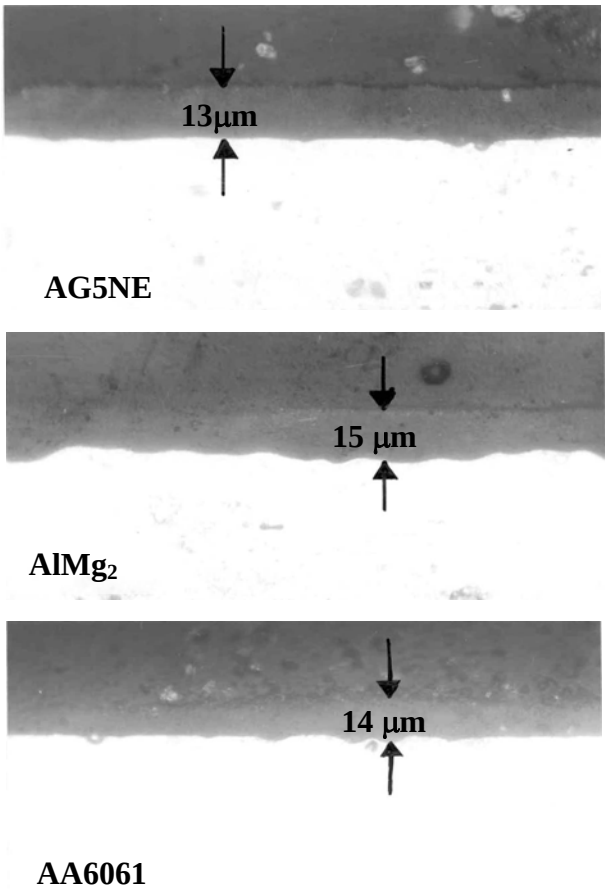

Fig. 7.8. Boehmite layers on various Al cladding alloys irradiated in ORR for ~300d, pH 5.5 - 6.5

Table 7.3 shows a collection of corrosion layer thickness data obtained during the RERTR fuel test programs carried out in various research reactors. The appearance of the corrosion layers is very similar to those shown in Fig. 7.8. No evidence of pitting has been observed, and where x-ray diffraction was performed, the corrosion was found to consist of a mixture of Bayerite and Boehmite. There appears to be no discernable difference in the corrosion behavior of the solution hardening Al-Mg alloys ($AlMg_2$, Ag_2NE, etc., which are

comparable to the 5000 type alloys) and the dispersion hardening alloys (SAV 1 and 6061). All cladding alloys were, because of the hot rolling and blister anneal procedures, in a fully annealed condition with, depending on the finishing fabrication step, a small (~10%) amount of cold work. None of the reactors employ pH reduction by coolant acidification, nor do they pre-film the cladding.

Table 7.3. Corrosion layer thicknesses on irradiated Al-clad dispersion fuels used without pre-filming with aluminum hydroxide.

Reactor	Alloy	Thickness (μm)	Water pH	Coolant outlet Temp. (ºC)	Surface Heat flux (W cm^{-2})
ORR	AlMg2 AG3NE 6061	24 20 24	5-6.3	53	120
HFR	AG5NE	45	6.70	55	120
RGAS	AIMg2	40	6.5-7.0	54	60
NRU	6102	35	5.5-6.5	70	250
JMTR	AlMg2	20	5.5-6.0	45	100
IVV-2M	AlMg2 SAV-1	25	6	40	70
RA3	6061	12	5.0-6.2	35	40
OSIRIS	AG2NE	35	6	47	130

We may conclude from this experience that in reactor corrosion is not a fuel performance issue in any of these varied reactors if, as is the case for all listed in Table 7.3, coolant water purity is maintained by de-ionization, within a narrow pH range and at low conductivity values. At heat fluxes typical of the reactors in Table 7.3, the cladding temperature is only modestly increased by the presence of the corrosion product. However, for higher-power-density reactors such as the ATR, corrosion was recognized early as a potential performance issue. The ATR (and SRS production reactors) have been operated quite successfully by pre-treating the fuel cladding with a very thin, highly crystalline layer of boehmite. This layer minimizes the temperature differential across the hydroxide layer, eliminates spalling, and helps preclude significant additional hydroxide growth during irradiation.

An example of the efficacy of pre-filming is shown in Fig. 7.9 for the RERTR tests performed in ATR. Test plates in RERTR-1 and 2 were not pre-filmed and experienced severe corrosion-erosion and occasional pitting whereas the pre-filmed RERTR-3, 4 and 5 test plates showed uniform adherent and thin boehmite layers over the clearly visible fuel regions.

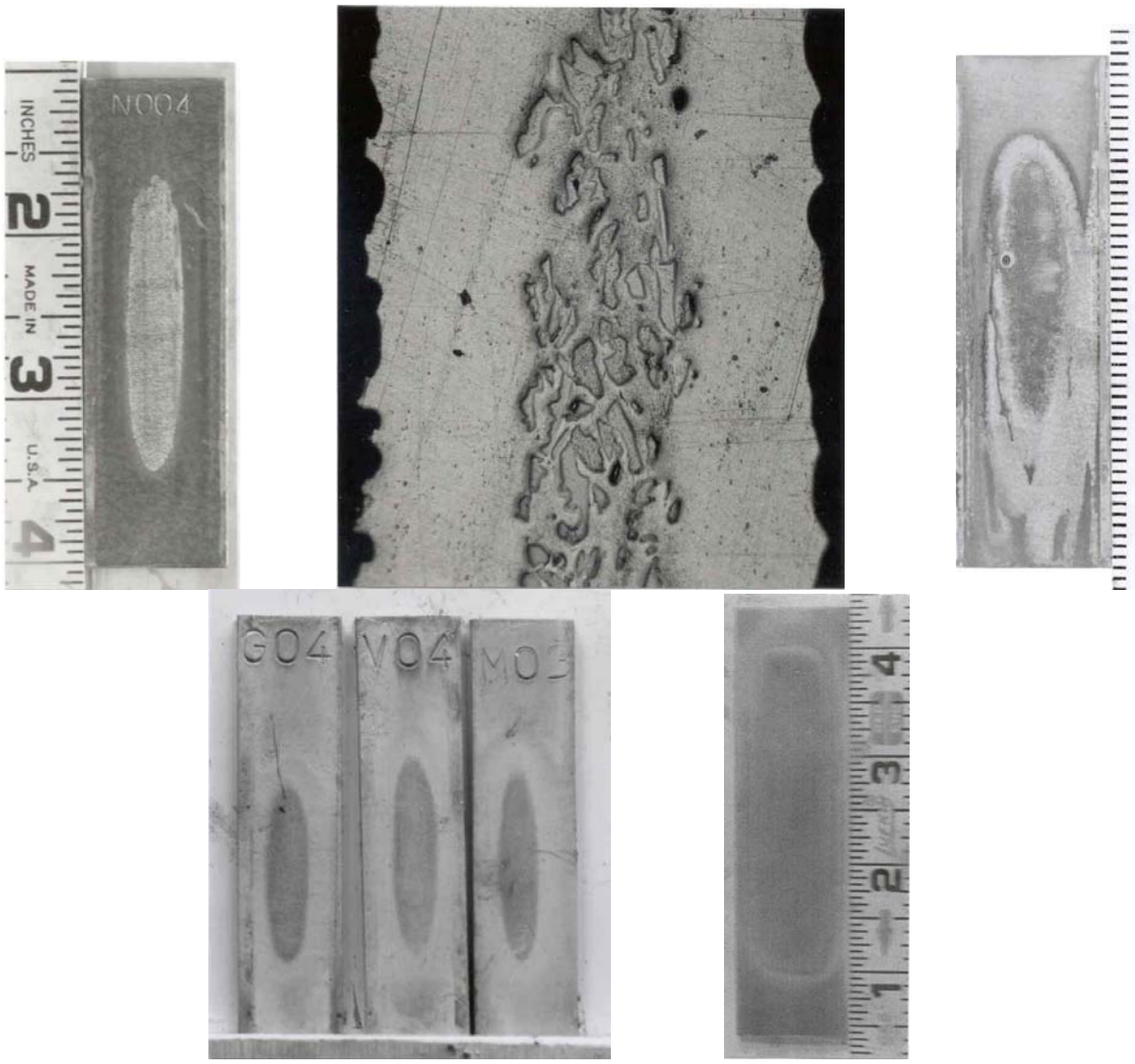

Fig. 7.9. Aluminum cladding corrosion, upper: untreated RERTR-2; lower: Prefilmed RERTR-3 and 4.

Oxide thickness prediction models

There are three primary models available in the literature for oxide thickness predictions. All of them are power-law models and were developed for data from out-of-pile loop tests. Because of the limitations in their original data, these models have limited ranges of applicability; for example, all of them were intended to be used at a single pH, which is pH (5), and restricted flow rate. In addition, irradiation effects were not considered in these models.

The rate equation for oxide growth on aluminum metal or alloy can be expressed by

$$\frac{dx}{dt} = k\, x^{-p} \tag{7.1}$$

where x is the film thickness, t time, k is a rate constant, and p the rate law power. The existing models use this rate equation. The integration of Eq. (7.1) gives the general form of the kinetic equation of aluminum alloy corrosion:

$$x = \left[{x_0}^{p+1} + (p+1)\, k\, t \right]^{\frac{1}{p+1}} \tag{7.2}$$

where x_0 is the film thickness at time zero.

The Griess model was developed in the1960s [9, 10]. It used the kinetic equation given in Eq. (7.2) with p=0.28535, after fitting p with their loop test data:

$$x = \left({x_0}^{1.28535} + 1.28535\, k\, t \right)^{0.778} \tag{7.3}$$

where

x = film thickness in μm at time t
x_0 = film thickness in μm at time zero
t = time in hr.

The rate constant k was expressed by

$$k = 1.2538 \times 10^5 \exp\left(\frac{-5913}{T_{x/c}} \right) \tag{7.4}$$

where $T_{x/c}$ = temperature at the oxide-water interface (or cladding surface temperature) in K. In their work, the temperature at the oxide-water interface and the cladding surface temperature are the same so they are used interchangeably.

As seen in Eq. (7.4), the rate constant is only dependent on the temperature at the oxide-water interface. The other variables, which affect the growth rate, were assumed to be fixed. Therefore, the Griess model is only applicable for cases that have pH 5, water flow rate of ~12 m/s and duration of 10 - 20 days.

The Kritz model [11] has the same kinetic equation as the Griess model, i.e., Eq. (7.3). The rate constant, however, was varied by raising the heat flux termto the power of 1.28535 as well as using a different pre-exponential constant and activation energy:

$$k = 8.686\, q^{1.28535} \exp\left(\frac{-2416.5}{T_{x/c}} \right) \tag{7.5}$$

where q is heat flux at the oxide-water interface in MW/m^2. The application range of the Kritz model is similar to that of the Griess model.

An updated version of ANS Correlation II was reported by Pawel, et al. [12-14]. They adopted the same kinetic equation given in Eq. (7.2) with p=0.351:

$$x = \left(x_0^{1.351} + 1.351\, k\, t \right)^{0.74} \tag{7.6}$$

The corresponding rate constant was

$$k = 6.388 \times 10^7 \exp\left(\frac{-9154}{T_{x/c} + 1.056\, q} \right) \tag{7.7}$$

Notice that the reaction temperature is increased by heat flux. The Pawel model also has an application range similar to the other models.

The reaction temperature of Griess and Kritz models is the temperature at the oxide-water interface although they use the rate constants fitted to the oxide thickness data. The reaction temperature of the Pawel model was obtained by adding a term linearly proportional to the heat flux to the oxide-water interface temperature. The reaction temperature of the Pawel model is independent of the oxide thickness and property. Since it relies on a constant proportionality on heat flux, this model tends to produce overpredictions for thin oxides and underpredictions for oxides thicker than ~20 μm. However, the inability of accounting for the effect of pH provides more reason for the discrepancies among the models.

The more recent model by Kim et al. [15] tried to overcome this disadvantage. This model uses a variable rate-law power by fitting data expressed in a function of oxide solubility:

$$\mathrm{p} = 0.12 + 9.22 \exp\left(-\frac{\mathrm{C_s}}{6.82 \times 10^{-9}} \right) \tag{7.8}$$

where C_s is given by

$$\ln \mathrm{C_s} = -\left(-13.79 - \frac{1211.16}{\mathrm{T_{x/w}}} \right)\left(0.041\mathrm{H}^2 - 0.41\mathrm{H} - 0.07 \right) \tag{7.9}$$

where the oxide solubility is in g/g of water, $T_{x/w}$ the oxide-water interface temperature in K and H is the pH.

The reaction temperature governing the Al oxidation reaction in steam is known to be the metal-oxide interface temperature [16]. In this situation, the oxidant transport through the oxide is the reaction controlling process. For thin oxides, since ΔT across the oxide film is small, the use of oxide-water interface temperature ($T_{x/w}$) as the reaction temperature is considered acceptable. However, this will cause a considerable underprediction in the oxide thickness calculation for a situation with a high ΔT, which prevails for a thick oxide with high porosity and a high heat flux.

To modify the reaction temperature, the temperature difference across the oxide film is added with a fitting adjustment to consider the porous nature of the oxide. The effect is correlated in the reaction constant k as follows:

$$k = 3.9 \times 10^5 \exp\left(\frac{-6071}{T_{x/w} + AB\frac{q\,x}{k_T}} \right) \tag{7.10}$$

where $T_{x/w}$ is the oxide-water interface temperature in K, q is the surface heat flux in MW/m^2, x in μm, and k_T in W/m-K. The pre-exponential factor and activation energy were fitted to the out-of-pile data available in the literature. The augmentation factor, A, is added as a multiplier to take into consideration the effect of coolant velocity. The augmentation factor increases as the coolant velocity increases, as can be seen in Eq. (7.10).

$$A = 0.43 + \frac{3.21}{1 + \exp\left(-\frac{v_c - 13.39}{3.60} \right)} \tag{7.11}$$

where v_c is the coolant flow rate in m/s.

Because of the water access through the defected oxide, the effective distance that the oxidant migrates through the oxide to the metal-oxide interface decreases. A correction factor, B, is needed to account for the reduction in the 'oxide thickness' for oxidant migration. The data fitting of in-pile data resulted in B=0.37 when the time interval in fitting Eq. (7.10) was set to 24 h, and the value of x at the previous time step was used to avoid endless iteration.

The Griess data were obtained for alloy Al 6061 and Al 1100, the Kritz data were for Al 8001, and the Pawel data were for pure Al, Al 1100, Al 6061 and Al 8001. The authors found no significant difference in the oxidation rate of these alloys, although different behavior associated with spalling and internal reactions was observed. Some European reactors use AG3NE (3%Mg+Al balance) and US reactors issue typically Al 6061 (1%Mg+Al balance) while Russian designed reactors use so-called SAV-1 alloy which is similar to Al 6061. There exists no discernable effect with respect to alloy types on the oxide thickness.

Other parameters that have an indirect effect on the oxidation rate were coolant electrical conductivity and coolant inlet temperature. None of these parameters are incorporated explicitly in any of the models.

7.5 References for section 7

1. McCoy, H.E., Weir, J.R., Influence of Irradiation on the Tensile Properties of the Aluminum, ORNL-TM-1348 (1966).
2. Marchbanks, M.F., ANS Materials Databook, ORNL/M-4582 (1995)

3. Farrell, K., Assessment of Aluminum Structural Materials for Service Within the ANS Reflector Vessel, ORNL/TM-13049 (1995).
4. Hofman, G.L., Personal communication, January (2003).
5. Walker, V.A., Graber, M.J., Gibson, G.W., ATR Fuel Materials Development Irradiation Results – Part II, USAEC report IDO-17157 (1966).
6. Eric Shaber and Gerard Hofman, "Corrosion Minimization for Research Reactor Fuel," INL/EXT-05-00256 (June, 2005).
7. Wefers, K., and Misra C., Oxides and Hydroxides of Aluminum, AlCOA Laboratories Technical Paper No. 19, Revised, 1987.
8. Byalobzheskii, A.V., Izdatel stvo Nauka, Moskva, 1967, Translated 1970 as AEC-TR 7096, p.17.
9. J.C. Griess, H.C. Savage and J.G. Rainwater, et al., ORNL-3230, Oak Ridge National Laboratory (1961).
10. J.C. Griess, H.C. Savage and J.L. English, ORNL-3541, ORNL-3230, Oak Ridge National Laboratory (1964).
11. R.S. Ondrejcin, DPST-83-324, Savannah River Laboratory (1983).
12. R.E. Pawel, G.L. Yoder, D.K. Felde, B.H. Montgomery and M.T. McFee, Oxidation of Metals, 36(1/2), 175 (1991).
13. R.E. Pawel, D.K. Felde, J.A. Clinard and T.A. Thornton, Corrosion 93, The NACE annual conference and corrosion show, 188/1 (1993).
14. S.J. Pawel, D.K. Felde and R.E. Pawel, Oak Ridge National Laboratory, Report ORNL/TM-13083, October, 1995.
15 Yeon Soo Kim, G.L. Hofman, A.B. Robinson, J.L. Snelgrove, N. Hanan, J. Nucl. Mater, 378 (2008) 220.
16 D.R. Dickinson, R.J. Lobsinger, HW-77529, Hanford Laboratory, 1963.

Intentionally Blank Page

SECTION 8 (U, Mo)Al DISPERSION FUEL PROPERTIES

8.1 Thermal Conductivity

The most important element of the temperature calculations made for U-Mo fuel plate irradiations is the evaluation of the fuel meat thermal conductivity. For example, for dispersion fuels, as fuel-matrix interaction proceeds, volume fractions of the meat constituents change significantly. The volume fraction of the low-conductivity reaction product phase is initially zero, but increases during irradiation. Conversely, the high-conductivity matrix phase in the meat decreases from its as-fabricated value as it is consumed by fuel-matrix interaction, by its incorporation into solution with the unreacted fuel alloy, and by extrusion out of the fuel meat region owing to the growth and swelling of the other phases. The fuel-phase mass is also consumed by fuel-matrix interaction; however, the volume of unreacted fuel can increase owing to decreases in density resulting from fission-product swelling and from the incorporation of aluminum into solid solution with the fuel alloy. In addition, fabrication porosity and fission-product porosity generated during irradiation in the fuel and reaction product phases affect the meat thermal conductivity. The effective fuel-meat thermal conductivity can be evaluated at any particular point in time if the constituent volume fractions are known; this can be done by using an analytical model for the thermal conductivity of a multiphase material where conductivities of the constituent phases are assumed known.

A multiphase conductivity model was derived for a two-phase material from purely theoretical considerations by Hashin and Shtrikman [1]. The matrix aluminum constitutes one phase, and the fuel (assumed to be spherical fuel particles surrounded by a uniform spherical shell of reaction-product) constitutes the other. The uniform reaction-product layer on the surface of the fuel particle produces a thermal resistance to radial heat flow out of the sphere that increases with time as the reaction-product thickness increases. This thermal resistance is calculated analytically and used to decrease the effective fuel-alloy thermal conductivity accordingly. The revised value for the fuel thermal conductivity is then used in the multiphase conductivity model to evaluate the effective meat thermal conductivity.

The analytical model of Hashin and Shtrikman calculates an upper and lower bound to the effective thermal conductivity of the multiphase material. A modified form of the Hashin and Shtrikman relation that allows for a smooth transition between the upper and lower bounds as a function of the fuel-phase fraction [2] is given as:

$$k_{meat} = -f + 3Vf + 2m - 3Vm + \frac{\sqrt{8\,fm + \left(f - 3Vf - 2m + 3Vm\right)^2}}{4}\ , \tag{8.1}$$

where k_{meat} is the effective thermal conductivity of the fuel meat, f is the composite thermal conductivity of the fuel and reaction-product phase, m is the thermal conductivity of the matrix phase, and V is the sum of the volume fractions of the fuel and reaction-product phases. The effective meat thermal conductivity of Eq. (8.1) is labeled ‘autocoherent conductivity’ and shown plotted for a U-10Mo/Al dispersion fuel as a function of fuel volume loading in Fig. 8.1. Also shown in the Fig. are measured thermal conductivities, showing that the model’s predictions are in excellent agreement with measured values.

The effect of porosity on thermal conductivity is treated by using a porosity correction factor applied to the base thermal conductivity of the phase that contains the porosity (i.e., the unreacted U-Mo alloy or the aluminide reaction-product). For meat porosity resulting from fabrication, the porosity correction factor is applied to the effective meat thermal conductivity as [3]:

$$k_P = k_{100} \cdot \exp(-2.14P) \ , \tag{8.2}$$

where k_p is the thermal conductivity of the porous materials, k_{100} is the thermal conductivity of the fully-dense material, and P is porosity. This porosity correction factor is valid for porosities below 0.30.

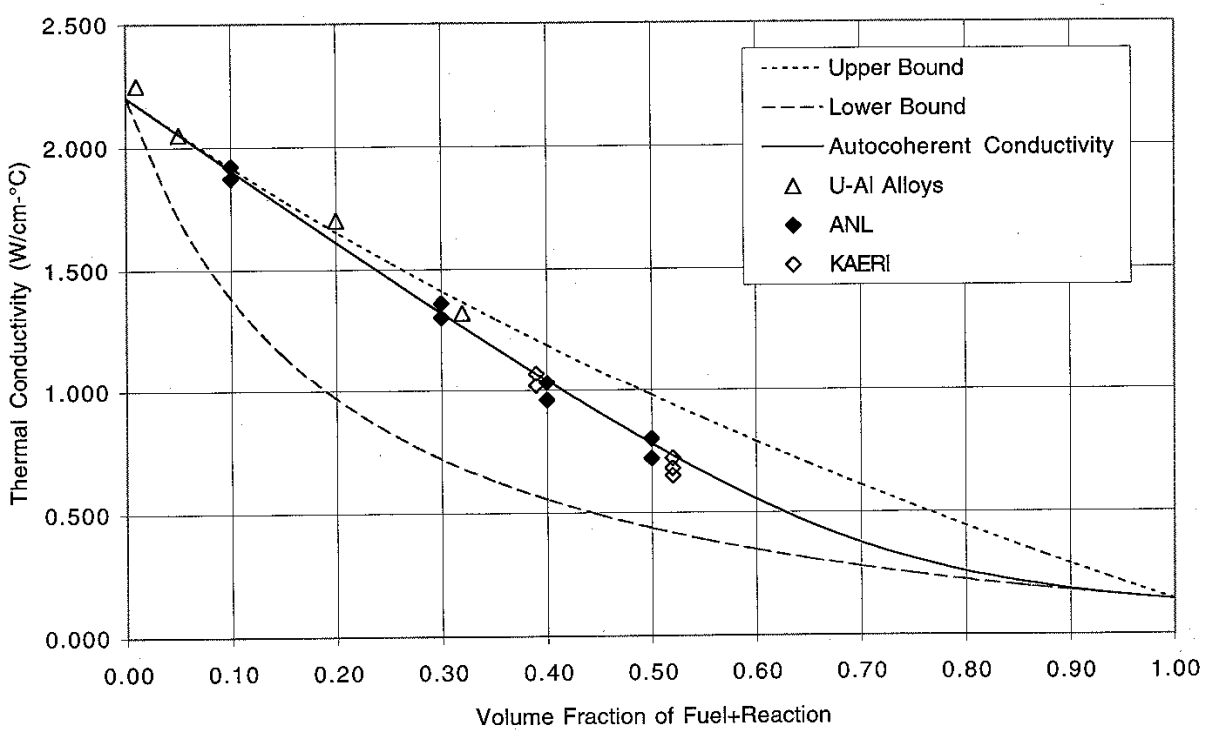

Fig. 8.1. Dispersion fuel thermal conductivity model compared to measured data.

8.2 Thermal Expansion

Data on the thermal expansion behavior of U-Mo dispersion fuels produced by rolling or extrusion are not available in the literature. Hofman and Snelgrove [4]discuss available data for U-Al alloy fuels and UAl_4-Al dispersions in a recent review, and come to the conclusion that elastic restraint due to the fuel particles does have an effect on the thermal expansion coefficient of the fuel meat, reducing it somewhat from that of aluminum. It might be expected that the thermal expansion coefficient of aluminum clad fuel plates would be similar to that of aluminum, which represents more than 2/3 of the plate volume at beginning of life.

8.3 Fuel-Matrix Interaction

The interaction layer (IL) thickness data of the plates with the Si-added Al matrix were available from RERTR-6 and 7A. The IL growth kinetics of plates with 2wt% or more Si in the Al matrix was drastically lower than the pure-Al matrix plates. The correlation has the same functional form as for pure-Al matrix plates with different fitting constants [5].

$$Y^2 = A\ F_r^{\ 0.5}\ \exp\left(-\frac{Q}{RT}\right) t \tag{5}$$

where Y is the IL thickness in cm, F_r the fission rate in f/cm^3-s, T temperature in K, and t time in s.

Fitting the measured data from RERTR-6 and 7A was performed in the PLATE code [3] by iteration. As a result, $A=7.5\text{x}10^{-18}$ and Q=8000 cal/mol were obtained. This compares the pure-Al matrix plates, for which $A=5\text{x}10^{-17}$ and Q=7000 cal/mol [6].

8.4 Contact Ratio and Matrix Extrusion

The use of a contact ratio for those phenomena that depend on the available surface area between the fuel and matrix phases is an important calculational detail. The surface area available for fuel-matrix interaction decreases as the matrix phase depletes. To account for this effect, a semi-empirical contact ratio correlation [7, 8] is used:

$$C_R = 4.005\times10^{-3}\,V - 3.432\times10^{-5}\,V^2 + 9.206\times10^{-7}\,V^3, \tag{8.4}$$

where C_R is the contact ratio and V is the sum of the volume fractions of the unreacted fuel and reaction-product phases.

Extrusion of matrix aluminum out of the fuel meat region during irradiation may be caused by the in-growth of the brittle reaction-product phase and fuel swelling. Extrusion of a contiguous matrix phase occurs out of the center regions of the fuel plate and toward the fuel surface. Extrusion occurs as long as the matrix phase is contiguous, currently defined as a matrix volume fraction of 0.25 or greater; once this limit on matrix volume fraction is reached, it is assumed that the remainder of the matrix phase is pinned and no further extrusion is allowed.

8.5 Strength of As-Fabricated Dispersions

Sumpter [9] determined compressive yield strength (0.2% offset) of 6061 clad plates containing a 51 wt.% U_3O_8 dispersed in an X8001 aluminum matrix. The cladding was in the O-temper condition. Test temperatures ranged from 24-260°C. Results (Fig. 8.2) show that the dispersion fuel plates exhibit a substantial increase in compressive yield stress over 6061 aluminum blanks. This is especially true at higher temperatures; above 150°C, 6061-O begins to exhibit a rapid decrease in yield strength, falling from approximately 55 MPa (8000 psi) at 150°C to 31 MPa (4500 psi) at 260°C, a decrease of 44% in a range of 110°C. In contrast, the dispersion fuel specimens at 150°C had a considerably higher compressive yield strength of 78 MPa (11,300 psi) and retained 90% of their strength on increasing the test temperature to 260°C.

Tensile properties of a 33 wt.% dispersion of U_3O_8 in X8001 aluminum clad by 6061 aluminum in the O-temper condition were reported by Martin and Wier [10] and plotted in Fig. 8.3. As is the usual case, the dispersion has a yield strength markedly higher than that of 6061-O aluminum. Total elongation at failure, a measure of ductility, is in the range of 5-9%, and did not exhibit any definite temperature dependence. Elongation to failure is 20-30% for 6061 in the same nominal heat treat condition over the same temperature range. Because of the differences in test method, the data of Sumpter are difficult to compare directly to that of Martin and Wier.

Some relevant tensile strength data were recently generated by KAERI (Korea Atomic Energy Research Institute) [11] for rod-type U-Mo dispersion fuel meats fabricated by extrusion. These data are shown in Fig. 8.4. Fig. 8.4 shows the dependence of ultimate tensile strength and elongation to failure as a function of particle volume loading for dispersions of irregular (denoted by 'com.' For comminuted in the figure.) and spherical particles of U-Mo alloys. According to these data, the strength of the fuel meats increases with increasing fuel volume loading. As might be expected, ductility decreases with increasing fuel loading.

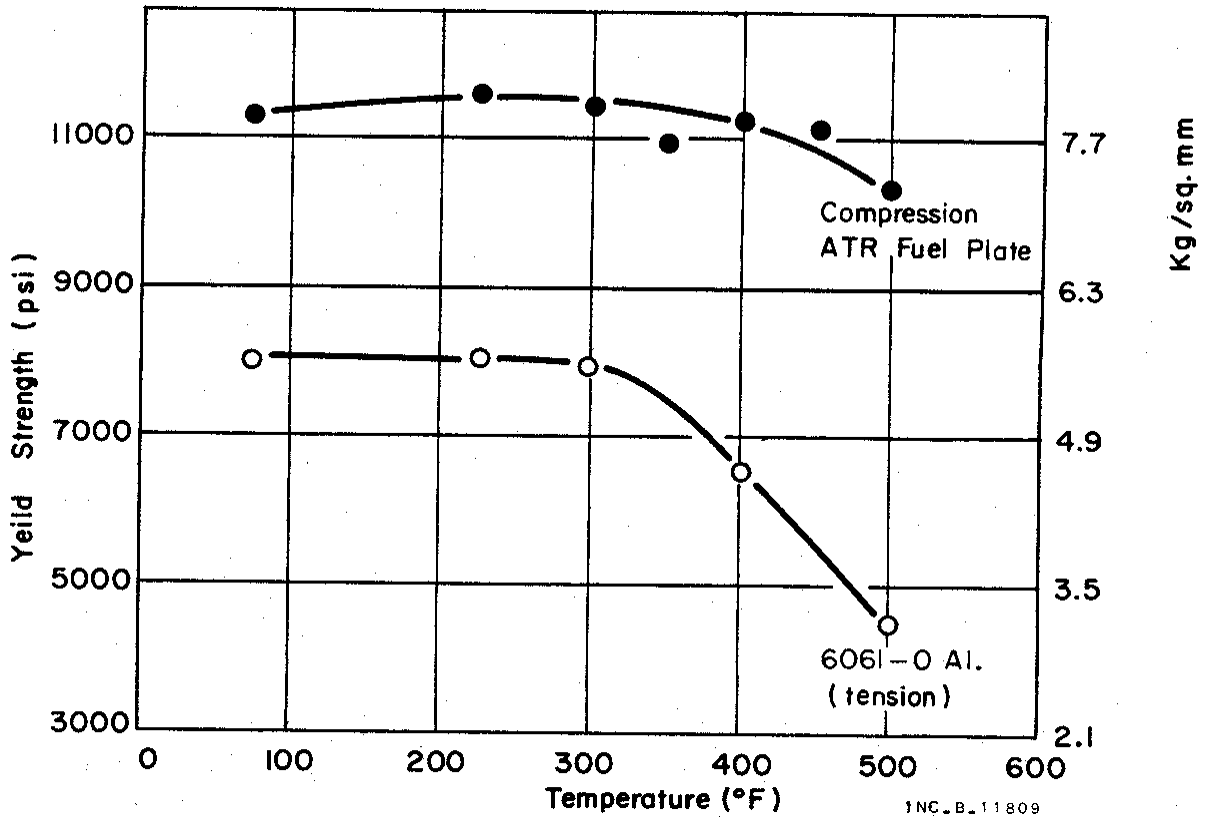

Fig. 8.2. Compressive yield strength (0.2% offset) of unirradiated 6061 clad plates containing a 51 wt.% U_3O_8 dispersed in an X8001 aluminum matrix. Cladding is in the O-temper condition. [10].

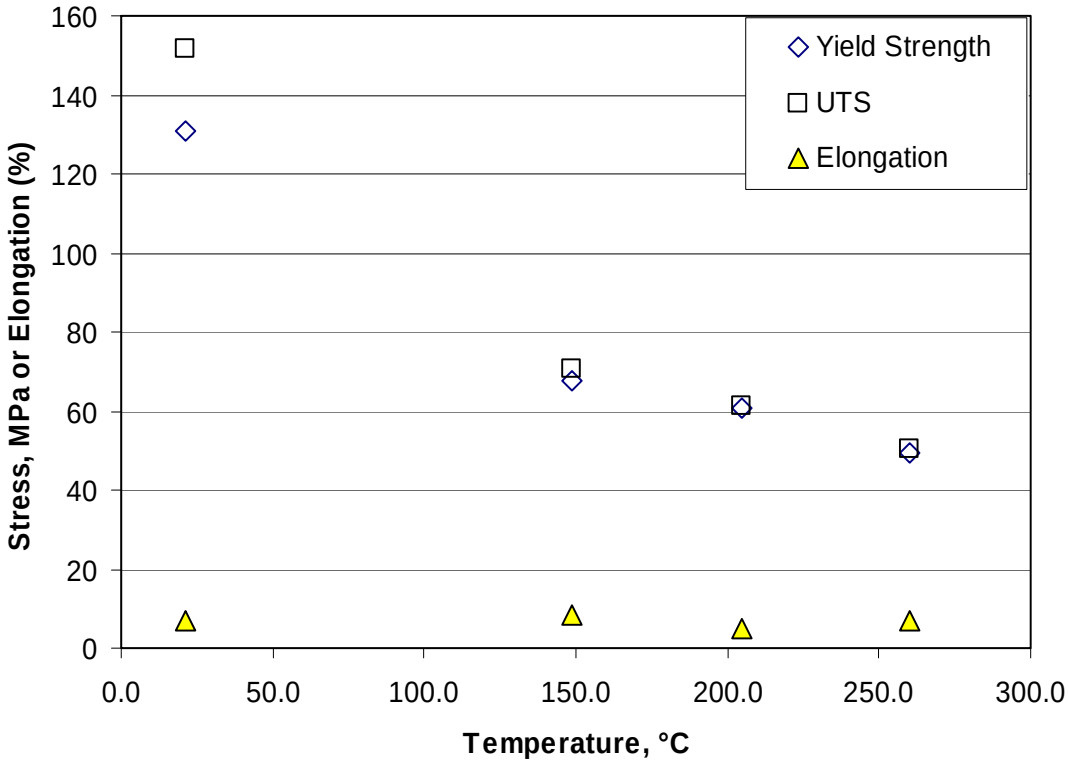

Fig. 8.3. Tensile yield and ultimate tensile strength data for a 33 wt.% dispersion of U_3O_8 in X8001 aluminum as reported by Martin and Wier [10]. Cladding is 6061 aluminum in the O-temper condition. Elongation at failure is also plotted.

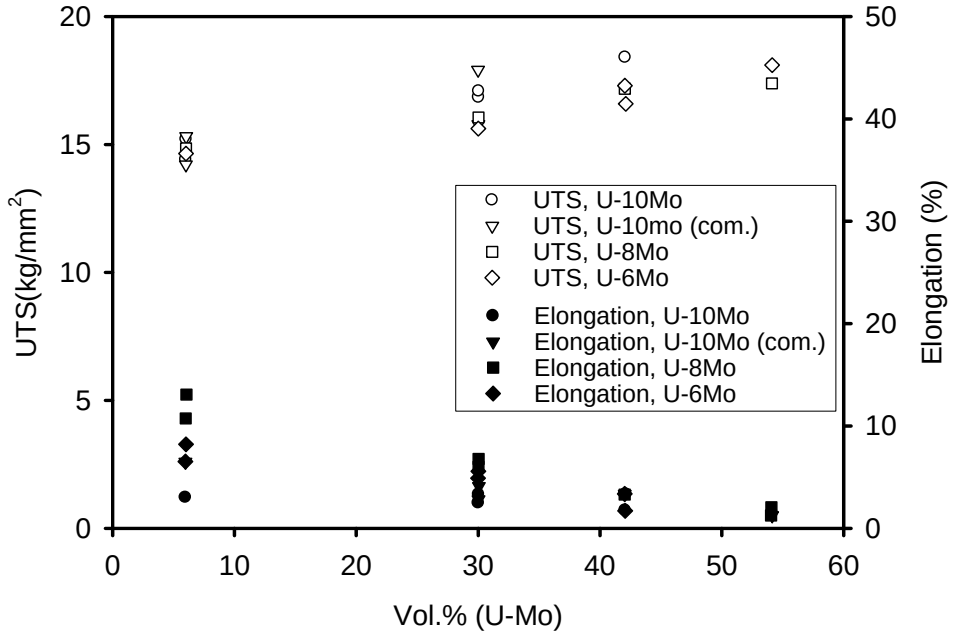

Fig. 8.4. Tensile strength and elongation data for extruded U-Mo/Al fuel meats as a function of U-Mo volume loading.

8.6 Elastic Modulus of Dispersion Fuels

Rule of mixture predictions can be made for the elastic moduli of particulate composite materials. Upper and lower bounds for the modulus are represented by Eqs. (8.5) and (8.6), respectively [11].

$$E_c = E_m V_m + E_v V_p \quad \text{upper bound,} \tag{8.5}$$

$$E_c = \frac{E_m E_p}{V_m E_p + V_p E_m} \quad \text{lower bound,} \tag{8.6}$$

where E is the elastic modulus, V is the volume fraction, and the subscripts m and p refer to the matrix and particulate phases. Sumpter presented Young's modulus data derived from stress/strain curves. The modulus of the dispersion was found to be slightly higher than that of aluminum blanks, and fell off more slowly with temperature, due to the presence of the higher-modulus reinforcing phase.

8.7 Strength of Irradiated Dispersion Fuels

Most strength data for irradiated dispersion fuels have been collected from fuel specimens clad in 1100 and X8001 aluminum. Fewer data on the mechanical properties of irradiated fuel plates clad with contemporary precipitation hardening 6061 and solution hardening AG3NE alloys appear in the literature. Both tensile and compressive test data are available for UAl_x and U_3O_8 plate-type dispersions in the as-fabricated state and as a function of neutron fluence. No new published data on irradiated fuel have been generated since a review by Snelgrove and Hofman [4] published in 1994. This section borrows heavily from that most recent review.

Results from mechanical testing of irradiated fuel plates have been reported by Graber [12] and Dittmer [13]. Dittmer compression tested both cold worked 35 wt.% (vol. %) UAl_x clad with 1100-H12 aluminum (Engineering Test Reactor type) and plates containing a 51 wt.% dispersion of UAl_x clad in 6061-O aluminum. Dittmer found that the compressive yield strength of the 6061 clad 51 wt.% UAl_x dispersions increased with fission density in the range of $0.2 - 1.4 \times 10^{27}$ m^{-3} at temperatures in the range of 204°-316°C as shown in Fig. 8.5. In contrast, the cold worked 1100 series clad ETR plates decreased in strength.

Graber [13] reported that the postirradiation tensile strength of U_3O_8, UO_2, and UAl_3 dispersions varied with the cladding type and fuel loading dispersions containing 50 wt.% UAl_3 generally exhibited a decrease in tensile strength on irradiation at a test temperature of 204°C, independent of whether the plates were clad in 6061 or X8001 alloy. In contrast, UO_2 and U_3O_8 plates loaded at 22-30 wt.% and clad in 1100 series aluminum showed an increase in strength under the same testing conditions.

Application of these results to U-Mo dispersion fuel plates is difficult due to the obvious sensitivity of these data to strength testing method, cladding material, fuel volume loading, and fuel type. The degree of reaction and the type of interaction product formed during irradiation will have a significant impact of the tensile strength of the fuel meat. Operation of fuel plates at fuel densities on the order of 6-7 $g{\cdot}U/cm^3$ will result in a significant depletion of matrix aluminum to form a mass of $(U\text{-}Mo)Al_x$ reaction product with unknown properties surrounding unreacted U-Mo fuel particles. Cracking observed in postirradiation micrographs suggests that the fuel meat of plates in this condition will not bear a significant tensile stress. In the absence of experimental strength data for U-Mo fuels, a lower bound for strength can be established by considering the strength of the cladding material alone. Intermetallic phases, however, may support a significant compressive load, and, as long as the fuel meat remains bonded to the cladding, the compressive yield strength of irradiated fuel plates may not be negatively affected.

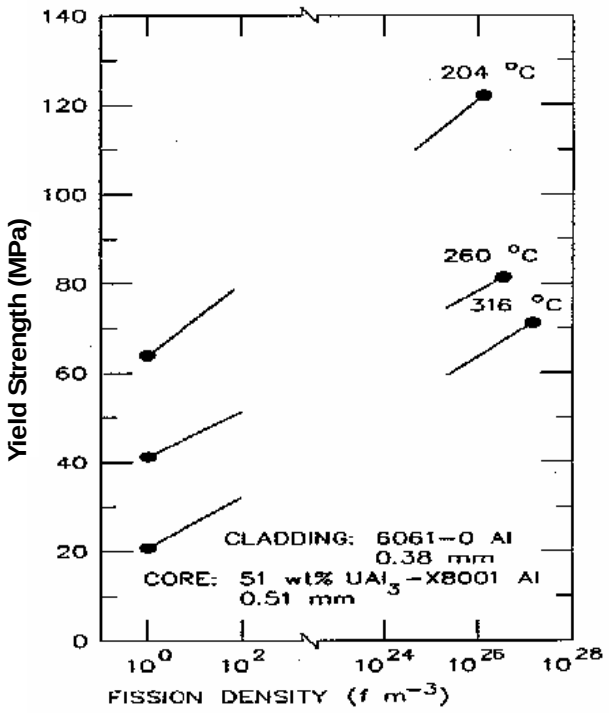

Fig. 8.5. Compressive yield strength of irradiated 51 wt.% UAl_3 fuel plates in comparison to unirradiated strength.

8.8 Hardness of Dispersants as a Function of Burnup

As shown in Fig. 8.6, the micro hardness of U-10 w% Mo initially increases rapidly with burnup to a constant value over a large burnup range after which it rapidly recovers to the preirrdiation value. This apparent loss of irradiation hardening correlates with a significant increase in porosity and grain refinement

.

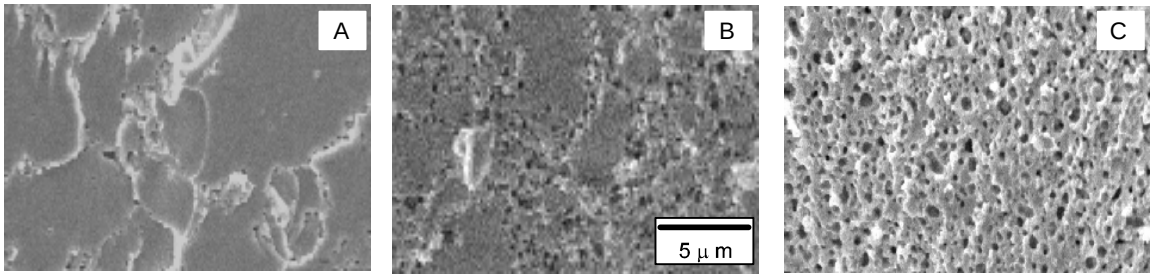

(a) (b) (c)

(a) Low burnup, only gas bubbles on grain boundaries, (b) medium burnup, grain refinement initiated, (c) high burnup, fully refined grains.

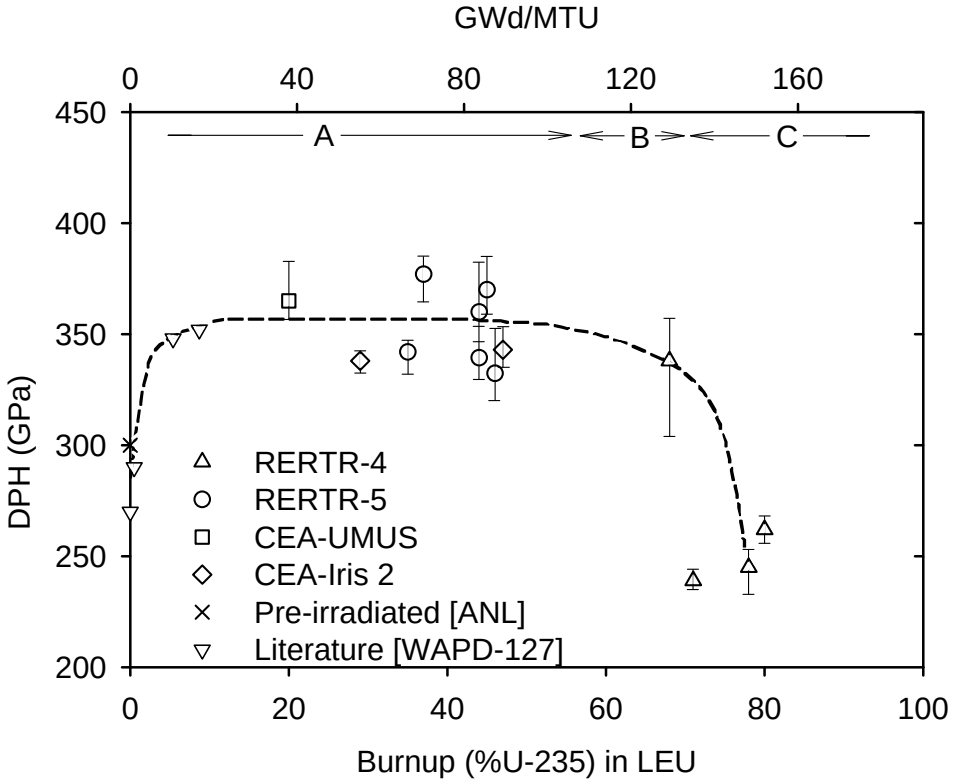

Fig. 8.6. U-Mo microstructure and microhardness changes with burnup. Microstructural stages classified as A, B, C in the photos correspond respectively to the regions in the graph.

8.9 References for Section 8

1. Z. Hashin and S. Shtrikman, "A Variational Approach to the Theory of the Effective Magnetic Permeability of Multiphase Materials," Journal of Applied Physics, Vol. 33 (1962) pp. 3125-3131.
2. David Plancq, Private Communication, CEA-Cadarache, France (2002).
3. M. E. Cunningham and K. L. Peddicord, "Heat Conduction in Spheres Packed in an Infinite Regular Cubical Array," International Journal of Heat and Mass Transfer, Vol. 24 (1981) pp. 1081-1088.
4. Snelgrove J.S and Hofman, G.L, Materials Science and Technology, VCH (1994)
5. Y.S. Kim, G.L. Hofman, H.J. Ryu, and S.L. Hayes, "Irradiation enhanced interdiffusion in the diffusion zone of U-Mo dispersion fuel in Al," J. Phase Equil. Diffus., 27 (2006) 614.
6. Y.S. Kim, G.L. Hofman, H.J. Ryu, et al., RERTR Meeting, 2007.
7. J. Gurland, "An Estimate of Contact and Continuity of Dispersions in Opaque Samples," Transactions of the Metallurgical Society of AIME, Vol. 236 (1966) pp. 642-646.
8. Y.S. Kim and G.L. Hofman, ANL Memo, Feb. 2006.
9. Sumpter, K.C., A Primary Study on the Compressive Properties of Composite Nuclear Fuel Plates, IN-1179, Idaho Nuclear Corporation (1968).
10. Martin, W.R., Weir, J.R., Mechanical Properties of X8001 and 6061 Aluminum Alloys and Aluminum-Base Fuel Dispersion at Elevated Temperatures, ORNL-3557, Oak Ridge National Laboratory (1964).
11. Kim, C.-K., Ryu, H.-J., Park, J.-M., Kim, K.-H., Kim, H.-R., Lee, K.-H., "Fabrication of Atomized U-Mo Dispersion Rod Type Fuel for Irradiation Test Related to the Qualification Program," Proc. Of the 2000 International Meeting on Reduced Enrichment for Research and Test Reactors, ANL/TD/TM01-12 (2001).
12. Graber, M.J., in Annual Progress Report on Fuel Element Development for FY 1963: Gibson, G.W., Graber, M.J., Francis, W.C. eds., Report IDO-16934 (1963).
13. Dittmer, J.O., M.S. Thesis, Idaho State University (1969).

Nuclear Engineering Division
Argonne National Laboratory
9700 South Cass Avenue, Bldg. 208
Argonne, IL 60439

www.anl.gov